Title
Modeling nonlinear optical microscopy in scattering media, part I. Propagation from lens to focal volume: tutorial.

Permalink
https://escholarship.org/uc/item/6q16h8tx

Journal
Journal of the Optical Society of America A: Optics, Image Science and Vision, 40(5)

Authors
Ranasinghesagara, Janaka
Venugopalan, Vasan
Potma, Eric

Publication Date
2023-05-01

DOI
10.1364/JOSAA.478712

Peer reviewed

Modeling nonlinear optical microscopy in scattering media, part I. Propagation from lens to focal volume: tutorial

Janaka C. Ranasinghesagara[1,2], **Eric O. Potma**[2,3], **Vasan Venugopalan**[1,2,*]

[1]Department of Chemical and Biomolecular Engineering, University of California, Irvine, California 92697, USA

[2]Beckman Laser Institute and Medical Clinic, University of California, Irvine, California 92697, USA

[3]Department of Chemistry, University of California, Irvine, California 92697, USA

Abstract

The development and application of nonlinear optical (NLO) microscopy methods in biomedical research have experienced rapid growth over the past three decades. Despite the compelling power of these methods, optical scattering limits their practical use in biological tissues. This tutorial offers a model-based approach illustrating how analytical methods from classical electromagnetism can be employed to comprehensively model NLO microscopy in scattering media. In Part I, we quantitatively model focused beam propagation in non-scattering and scattering media from the lens to focal volume. In Part II, we model signal generation, radiation, and far-field detection. Moreover, we detail modeling approaches for major optical microscopy modalities including classical fluorescence, multi-photon fluorescence, second harmonic generation, and coherent anti-Stokes Raman microscopy.

1. INTRODUCTION

Laser-scanning nonlinear optical (NLO) microscopy methods enable structural and functional visualization of thick cellular and tissue samples with sub-micrometer detail [1–3]. These methods rely critically on the formation of a well-defined focal spot within the tissue specimen. Light scattering in the tissue, however, distorts the amplitude and phase of the incident laser beam wavefront, which degrades the confinement of the diffraction-limited focal volume [4,5]. As a result, the focal volume within scattering samples is often expanded in both lateral and axial dimensions and generally accompanied by an overall reduction of light intensity in the focal region. This negatively impacts the imaging depth in the tissue, as well as image resolution and signal-to-noise ratio (SNR). Overcoming the effects of light scattering constitutes a grand challenge in optical microscopy with the purpose of improving imaging depth and resolution in thick tissue samples.

[*] vvenugop@uci.edu .

Counteracting the effects of scattering is challenging. Various adaptive optics approaches have been developed to compensate for wavefront distortions introduced by light scattering in the sample. A common compensation strategy is to modify the wavefront of the incident beam with a deformable mirror (DM) or spatial light modulator (SLM) to offset the optical aberrations caused by optical components and/or refractive index variations within the sample [6–8]. Optical aberrations can be largely canceled out by adjusting the incident wavefront with the conjugate of the phase aberration. Phase distortion due to the presence of discrete scatterers has been evaluated or sensed by various methods to determine the optimal phase compensation [8]. While these approaches have been successful in improving the magnitude and SNR of optical signals in laser scanning microscopy, the performance gains achieved thus far have remained rather modest [9,10]. In some cases, knowledge of the phase front is useful to compensate for scattering effects albeit at the expense of image acquisition speed. Many adaptive optics implementations for laser-scanning microscopy circumvent direct measurement of the wavefront entirely and apply phase compensation indirectly using iterative optimization of empirical parameters such as overall signal strength [11,12]. In some cases, this indirect optimization approach results in large errors [13].

The fundamental principles governing electromagnetic beam propagation and scattering are well established [14–17]. Therefore, it stands to reason that these principles can be utilized to comprehensively model and describe the effects of light scattering in laser-scanning optical microscopy. Such a model has the potential to provide fundamental insights into the factors that control the degradation of image resolution and depth within scattering media. Such a model would enable a comparative analysis of the relative sensitivity of different imaging modalities under similar scattering conditions. This approach would provide a rigorous basis for understanding the fundamental processes that contribute to wavefront distortion. This knowledge may then be leveraged to generate *a priori* information to dynamically synthesize wavefronts for adaptive optics applications.

Investigators have modeled various components of the optical microscopy process. One approach taken to model electromagnetic beam propagation in scattering media is to consider randomly distributed scatterers and apply a stochastic model [18–22]. Another approach is the use of convolutions with a 3D Green's function to calculate forward and backward scattered fields [23–25]. Such approaches may provide qualitative agreement with experimental observations, but they are unable to properly account for the amplitude and phase characteristics of propagating fields for specific scatterer configurations.

Numerical Maxwell's equations solvers such as the finite difference time domain (FDTD) or pseudo-spectral time domain (PSTD) methods are well suited for computing optical microscopy signals for specific scatterer configurations. While both FDTD and PSTD methods have been used successfully to model tightly focused beam propagation in scattering media [26–30], the process is complex and requires special techniques to define sources and minimize errors [31–34]. Moreover, these techniques require significant computational resources in terms of memory and run time, and scale with the total volume under consideration [35]. FDTD and PSTD methods also require near- to far-field (NTFF) transformation [36] to obtain the far-field results, which may be compromised by poor accuracy [37]. In contrast, the electromagnetic propagation tools that have been used

successfully to model stratified media [38,39] are limited to a few specific structures possessing a high degree of symmetry [40].

Several analytical field propagation methods have been developed to calculate the effect of scattering on tightly focused laser fields [41–47]. Most methods are limited to a single scatterer placed at a specific location [41–43]. Other methods [44,45] based on the T-matrix approach [48,49] with no adaptive optics corrections are limited in scope. The method developed by Török and co-workers [46] considers multiple spherical scatterers located proximal to the focal point and applies Mie theory to compute the scattered far field. Another approach, based on Huygens–Fresnel propagators [47], shares some similarities with the scattering calculations of [46] but has the advantage of considering the effects of interparticle scattering. Using Huygens–Fresnel propagators, we have developed a computational framework that simulates focused beam propagation, followed by the generation, radiation, and detection of nonlinear microscopy signals in media containing scattering particles at specific locations [50]. We utilize elements of this framework in this tutorial.

In this tutorial, we show how existing analytical electromagnetic field propagation methods can be synthesized into an integrated, comprehensive, modeling framework for NLO microscopy in scattering media. One important advantage of the analytical modeling framework presented here is that the computational cost does not depend on the volume of the computational domain, but rather on the number of scatterers and number of locations where we compute the field. Unless one wishes to model a system with thousands of scatterers, investigators can implement and execute the methods provided in this tutorial using a desktop/laptop computer.

In Part I of this tutorial, we consider a basic optical microscope configuration with aberration-free aplanatic lenses as shown in Fig. 1. The incident beam traverses the aplanatic lens and propagates toward the focal region in either a scattering or non-scattering medium. We present the methods used to model electric field propagation. Specifically, we formulate the mathematical representation of the incident beam in Section 2 and the lens output in Section 3. In Section 4, we present and analyze several electromagnetic approaches that can be utilized to compute focal fields in non-scattering media. In Section 5, we describe methods to model the effects of discrete scatterers in the medium and compute the resultant scattered fields proximal to the focal region. In Part II of this tutorial [51], we show how to calculate the electric field distribution near the focal volume and use these results to compute the resulting induced nonlinear polarization within the sample. In addition, we treat signal radiation from the focal volume in the direction of the detector in scattering media and describe a method for displaying far-field data and continuous propagation of NLO signals in a 4 f system. We conclude by providing case studies that illustrate results obtained at each stage of this modeling process for second harmonic generation (SHG) and two-photon excitation (TPE) microscopy.

2. INCIDENT BEAM FORMULATION

We begin by considering a collimated incident beam $\mathbf{E}^{\text{inc}}(x_\infty, y_\infty)$ that propagates in a direction parallel to the optical axis. Using the Jones vector representation [52,53], the incident beam can be expressed as

$$\mathbf{E}^{\text{inc}}(x_\infty, y_\infty) = \begin{bmatrix} E_x^{\text{inc}} \\ E_y^{\text{inc}} \\ E_z^{\text{inc}} \end{bmatrix} = \begin{bmatrix} A_x(x_\infty, y_\infty) \exp(i\psi_x) \\ A_y(x_\infty, y_\infty) \exp(i\psi_y) \\ 0 \end{bmatrix}, \tag{1}$$

where $\left[E_x^{\text{inc}}, E_y^{\text{inc}}, E_z^{\text{inc}} \right]$ are the Cartesian electric field components of $\mathbf{E}^{\text{inc}}$. $A_x(x_\infty, y_\infty)$ and $A_y(x_\infty, y_\infty)$ are amplitudes of the x and y electric field components, respectively, at the locations (x_∞, y_∞), which span the plane perpendicular to the z axis. ψ_x and ψ_y represent the phase of each component. Note that Eq. (1) is valid for collimated beams with the entrance pupil at infinity and does not apply generally to non-collimated incident beams.

A. Linearly and Circularly Polarized Beams

For an axisymmetric linearly or circularly polarized beam, we can rewrite the incident beam introduced above as [40,53]

$$\mathbf{E}^{\text{inc}}(x_\infty, y_\infty) = A_0(x_\infty, y_\infty) \exp(i\psi)\, \mathbb{BS} \cdot \mathbb{PV}, \tag{2}$$

where the $\mathbb{BS}$ matrix describes the characteristics of an ideal linear retarder (Babinet–Soleil compensator) [54] and $\mathbb{PV}$ is the input polarization vector. $\mathbb{BS} \cdot \mathbb{PV}$ represents the Jones vector [16]. $A_0(x_\infty, y_\infty)$ is the apodization function [55], and ψ and $A_0(x_\infty, y_\infty)$ represent the phase and amplitude, respectively, at the far-field pupil. As the phase ψ is the same for all electric field components, it can be safely ignored. The apodization function for beams of uniform amplitude or fundamental Hermite–Gaussian beam (HG00) mode with beam waist ω_0 can be expressed as [55]

$$A_0(x_\infty, y_\infty) = \begin{cases} 1 & \text{Flat} \\ \exp\left[-\left(x_\infty^2 + y_\infty^2\right)/\omega_0^2\right] & \text{HG00}. \end{cases} \tag{3}$$

In Eq. (2), the $\mathbb{BS}$ matrix facilitates the expression of polarized illumination [54,56]:

$$\mathbb{BS} = \begin{bmatrix} 1 & c & 0 \\ c & 1 & 0 \\ 0 & 0 & 1 \end{bmatrix}, \tag{4}$$

where $c = 0$ for linearly polarized illumination and $c = i = \sqrt{-1}$ for circularly polarized illumination. $\mathbb{PV}$, defined in terms of unit intensity, can be written as

$$\mathbb{P}\mathbb{V} = \begin{bmatrix} e_x \\ e_y \\ e_z \end{bmatrix}, \tag{5}$$

where $[e_x, e_y, e_z]$ for linearly x-polarized, linearly y-polarized, linearly $+45°$ polarized, linearly $-45°$ polarized, left-hand circularly polarized, and right-hand circularly polarized illuminations are given by $[1, 0, 0]$, $[0, 1, 0]$, $[1/\sqrt{2}, 1/\sqrt{2}, 0]$, $[1/\sqrt{2}, -1/\sqrt{2}, 0]$, $[1/\sqrt{2}, 0, 0]$, and $[0, 1/\sqrt{2}, 0]$, respectively.

B.   Incorporation of a Spatial Light Modulator

We can expand this basic framework by introducing a SLM into the light path prior to the incident lens. The SLM can be used to change the phase of the transverse field before entering the imaging system. The modified incident beam can be expressed as

$$\mathbf{E}^{\text{inc}}(x_\infty, y_\infty) = \mathbf{E}_{\text{SLM}}^{\text{inc}}(x_{\text{lm}}, y_{\text{lm}}) \exp(i\psi_{\text{lm}})\big|_{x_{\text{lm}}^2 + y_{\text{lm}}^2 \leq \frac{D^2}{4}}, \tag{6}$$

where $\mathbf{E}_{\text{SLM}}^{\text{inc}}(x_{\text{lm}}, y_{\text{lm}})$ represents the incident field on the SLM. Each (x_∞, y_∞) location within the incident field interacts with a corresponding $(x_{\text{lm}}, y_{\text{lm}})$ pixel of the SLM. ψ_{lm} is the phase angle provided by element (l, m) of the SLM. We consider a rectangular SLM with l rows and m columns. To adjust the phase within the entire beam using the SLM, the beam diameter D should be smaller than or equal to the SLM dimensions.

3.   LENS AND LENS OUTPUT

We consider an aberration-free aplanatic lens that we represent geometrically using a spherical surface. We will refer to this surface as the "spherical reference surface," and it is also known as a reference sphere [55] or a focal sphere [57]. For a flat wavefront, the radius of the spherical reference surface is f_1, which corresponds to the focal length as shown in Fig. 2. The size, curvature, and angular extent of the spherical reference surface are specified by the lens numerical aperture (NA) and focal length.

The lens output is determined by the electric field on the spherical reference surface, $\mathbf{E}^{\text{rs}}(\theta, \phi)$, which can be expressed as [53,55]

$$\mathbf{E}^{\text{rs}}(\theta, \phi) = \sqrt{\frac{n_{\text{inc}}}{n_{\text{m}}}} a(\theta) \mathbb{R}^{-1} \cdot \mathbb{I}_t \cdot \mathbb{L} \cdot \mathbb{R} \cdot \mathbf{E}^{\text{inc}}(x_\infty, y_\infty), \tag{7}$$

where n_{inc} and n_{m} are the refractive indices of the medium before and after the lens, respectively. The $\sqrt{\frac{n_{\text{inc}}}{n_{\text{m}}}} a(\theta)$ term is an apodization function that is introduced due to the radiometric effect and modifies the field amplitude [53,58–60]. Setting $a(\theta) = \sqrt{\cos\theta}$ specifies Abbe's sine condition [53,55,61] and provides optimal imaging in a plane perpendicular to the optical axis. For $a(\theta) = 1$, Herschel's condition is satisfied [53,59,60],

which provides only optimal imaging along a line segment, namely, along the optical axis. Unless stated otherwise, we will use the Abbe's sine condition because this condition is satisfied by the vast majority of microscopy imaging systems [53]. We consider a coordinate system where the origin lies at the focal point and the optical axis is collinear with the z axis.

It is helpful to define various transformation matrices. We define $\mathbb{R}$ to provide azimuthal rotation around the z axis [53,54]:

$$\mathbb{R} = \begin{bmatrix} \cos\phi & \sin\phi & 0 \\ -\sin\phi & \cos\phi & 0 \\ 0 & 0 & 1 \end{bmatrix},$$

(8)

where ϕ is measured from the $+x$ axis in the counterclockwise direction. $\mathbb{R}^{-1}$ in Eq. (7) transforms the electric field vectors back to the Cartesian basis. $\mathbb{R}^{-1}$ can be calculated by computing the transpose of $\mathbb{R}$ because $\mathbb{R}^T = \mathbb{R}^{-1}$.

We define the matrix $\mathbb{L}$ to provide the rotation around the axis that lies perpendicular to the meridional plane. $\mathbb{L}$ is used to account for the rotation of the field vector, i.e., the bending of the ray toward the axis. $\mathbb{L}$ is defined as [53,54]

$$\mathbb{L} = \begin{bmatrix} \cos\theta & 0 & -\sin\theta \\ 0 & 1 & 0 \\ \sin\theta & 0 & \cos\theta \end{bmatrix},$$

(9)

where θ is defined with respect to the $-z$ axis (Fig. 2). The matrix $\mathbb{I}_t$ provides the change in amplitude due to refraction at the lens/medium interface [53,54]:

$$\mathbb{I}_t = \begin{bmatrix} t_\parallel & 0 & 0 \\ 0 & t_\perp & 0 \\ 0 & 0 & t_\parallel \end{bmatrix},$$

(10)

where $t_\parallel$ and $t_\perp$ are parallel and perpendicular Fresnel transmission coefficients [40,53], respectively.

Equation (7) describes the effect of the lens on the incident electric field. The electric field on the spherical reference surface for a lens with a perfect anti-reflection coating ($t_\parallel = t_\perp = 1$) can be expressed as

$$\mathbf{E}^{\mathrm{rs}}(\theta, \phi) = \sqrt{\frac{n_{\mathrm{inc}}}{n_{\mathrm{m}}}} \frac{a(\theta)}{2}$$

$$\begin{bmatrix} (1 + \cos\theta) - (1 - \cos\theta)\cos 2\phi & -(1 - \cos\theta)\sin 2\phi & -2\sin\theta\cos\phi \\ -(1 - \cos\theta)\sin 2\phi & (1 + \cos\theta) + (1 - \cos\theta)\cos 2\phi & -2\sin\theta\sin\phi \\ 2\sin\theta\cos\phi & 2\sin\theta\sin\phi & 2\cos\theta \end{bmatrix}$$

$$\begin{bmatrix} E_x^{\mathrm{inc}} \\ E_y^{\mathrm{inc}} \\ E_z^{\mathrm{inc}} \end{bmatrix}. \tag{11}$$

Equation (11) provides a foundation for the focused beam propagation formulas that we provide in Section 4. Wherever $\mathbf{E}^{\mathrm{rs}}(\theta, \phi)$ is present, it can be replaced with Eq. (11) and the corresponding $\mathbf{E}^{\mathrm{inc}}$. For linearly and circularly polarized beams, we can determine $\mathbf{E}^{\mathrm{inc}}$ using the relationships described in Eqs. (2)–(5).

4. FOCUSED BEAM PROPAGATION IN NON-SCATTERING MEDIA

In this section, we examine three methods that, based on the information provided by $\mathbf{E}^{\mathrm{rs}}(\theta, \phi)$, can be used to compute field propagation to, and field distribution within, the focal volume for non-scattering media. The first method uses the Debye–Wolf integral (DWI), also known as the Richards and Wolf integral [40,57,62,63]. The DWI has been applied to a variety of focusing problems in homogeneous media including tightly focused fields obtained by focusing linearly polarized light [40,53–55,58]. The second approach is a solution obtained from Kirchhoff's vector integral (KVI) [53]. The KVI theorem is a solution to the wave equation, and it is the most frequently used diffraction integral in physical optics [15,53]. The third method is based on the Huygens–Fresnel principle (HFP), which describes electric field propagation between two points [15,64]. Solutions provided by the DWI are equivalent to the Fourier spectrum of the far field [55], and solutions from the KVI and HFP are based on fundamental electromagnetic theorems or principles [15,53].

A. Theory

1. Debye–Wolf Integral—The DWI provides the electric field at any observation location ρ as follows [40,53,57]:

$$\mathbf{E}(\rho) = \frac{-ikf_1}{2\pi} \iint_{\hat{u}_x^2 + \hat{u}_y^2 \leq 1} \mathbf{E}(\hat{u}_x, \hat{u}_y) \exp(ik\hat{\mathbf{u}} \cdot \rho) \frac{1}{\hat{u}_z} \mathrm{d}\hat{u}_x \, \mathrm{d}\hat{u}_y, \tag{12}$$

where $\rho = (\rho\cos\varphi, \rho\sin\varphi, z)$ is the observation location, proximal to the focal region (Fig. 2). $\hat{\mathbf{u}} = (\hat{u}_x, \hat{u}_y, \hat{u}_z)$ is a unit vector describing the direction of a ray [53]. This unit vector can also be expressed in terms of the wave propagation vector $\mathbf{k}$ as $\hat{\mathbf{u}} = (k_x/k, k_y/k, k_z/k)$, where $k_x = -k\cos\phi\sin\theta$, $k_y = -k\sin\phi\sin\theta$, $k_z = k\cos\theta$, and $k = 2\pi/(\lambda n_{\mathrm{m}})$. $\mathbf{E}(\hat{u}_x, \hat{u}_y)$ represents the electric field vector on the spherical reference surface. We can expand the vector dot product in the exponent and write

$$\widehat{\mathbf{u}} \cdot \rho = - \rho \sin \theta \cos(\phi - \varphi) + z \cos \theta. \tag{13}$$

The infinitesimal surface area on the reference sphere, expressed in Eq. (12) in terms of the unit vectors, can be rewritten in terms of the surface angles θ and ϕ as follows:

$$\frac{1}{\widehat{u}_z} \mathrm{d}\widehat{u}_x \, \mathrm{d}\widehat{u}_y = \sin \theta \, \mathrm{d}\theta \, \mathrm{d}\phi. \tag{14}$$

By substituting Eqs. (13) and (14) into Eq. (12) and replacing $\mathbf{E}(\widehat{u}_x, \widehat{u}_y)$ with $\mathbf{E}^{\mathrm{rs}}(\theta, \phi)$, the DWI in a homogeneous medium can be formulated as [40,53,55]

$$\mathbf{E}(\rho) = \frac{-ikf_1}{2\pi} \int_0^{\theta_{\max}} \int_0^{2\pi} \mathbf{E}^{\mathrm{rs}}(\theta, \phi) \times \exp\left\{ ikz \cos \theta - ik[(\rho \sin \theta \cos (\phi - \varphi)] \right\} \\ \sin \theta \, \mathrm{d}\phi \, \mathrm{d}\theta. \tag{15}$$

Note that Eq. (15) considers the phase of $\mathbf{E}^{\mathrm{rs}}(\theta, \phi)$ relative to the focal point. We can express the phase relative to the lens position by introducing a propagation phase $\exp(ikf_1)$ to Eq. (15) as

$$\mathbf{E}(\rho) = \frac{-ikf_1 \exp(ikf_1)}{2\pi} \int_0^{\theta_{\max}} \int_0^{2\pi} \mathbf{E}^{\mathrm{rs}}(\theta, \phi) \times \exp\left\{ ikz \cos \theta - ik[(\rho \sin \theta \cos \right. \\ \left. (\phi - \varphi)] \right\} \sin \theta \, \mathrm{d}\phi \, \mathrm{d}\theta. \tag{16}$$

Equation (16) is known as the angular representation of the focal field [55] and can be used to compute the focal electric field distribution.

2. Kirchhoff's Vector Integral Theorem—The KVI theorem considers the electromagnetic field following its passage through an aperture. Within this formulation, this electric field is expressed as [16,53,65]

$$\mathbf{E}(\rho) = \frac{1}{4\pi} \oint_{\mathscr{S}} \left[\mathbf{E} \frac{\partial G}{\partial |\widehat{\mathbf{u}}|} - G \frac{\partial \mathbf{E}}{\partial |\widehat{\mathbf{u}}|} \right] \mathrm{d}\,\mathscr{S}, \tag{17}$$

where G is a scalar Green's function and $\mathbf{E}$ represents the electric field. $\mathscr{S}$ is a closed surface that consists of surfaces A, B, and C, shown in Fig. 3 [66]. A represents the spherical reference surface, while B represents an opaque planar screen where both the field and its gradient are zero ($\mathbf{E} = 0$ and $\frac{\partial \mathbf{E}}{\partial |\widehat{\mathbf{u}}|} = 0$) [16]. C represents a large spherical surface with radius R^c that encloses the observation point ρ. A sufficiently large R^c is chosen such that ρ does not receive any contribution from C when the diverging field from ρ falls off sufficiently rapidly. Under these conditions, the contribution from the integral over C vanishes. This is also known as the Sommerfeld radiation condition. For more details, the reader is referred to

Section 8 of [16] or Section 3 of [64]. As the integrals over B and C have zero contribution, we can express Eq. (17) for surface A as

$$\mathbf{E}(\rho) = \frac{1}{4\pi} \int \int_A \left[\mathbf{E} \frac{\partial G}{\partial |\hat{\mathbf{u}}|} - G \frac{\partial \mathbf{E}}{\partial |\hat{\mathbf{u}}|} \right] \mathrm{d}A, \tag{18}$$

where G and $\mathbf{E}$ in the integrand of Eq. (18) are

$$G = \frac{\exp(ik|\mathbf{r}|)}{|\mathbf{r}|}, \tag{19}$$

$$\mathbf{E} = \mathbf{E}^{\mathrm{rs}}(\theta, \phi). \tag{20}$$

After applying Kirchhoff's boundary conditions, we can write

$$\left. \frac{\partial G}{\partial |\hat{\mathbf{u}}|} \right|_A = \left. \frac{\partial G}{\partial |\mathbf{r}|} \frac{\partial |\mathbf{r}|}{\partial |\hat{\mathbf{u}}|} \right|_A = -\frac{\exp(ik|\mathbf{r}|)}{|\mathbf{r}|} \left(ik - \frac{1}{|\mathbf{r}|} \right) \left(|\hat{\mathbf{u}}| \cdot \frac{\mathbf{r}}{|\mathbf{r}|} \right), \tag{21}$$

where $|\mathbf{r}|$ is given by

$$|\mathbf{r}| = \left[(x - x_0)^2 + (y - y_0)^2 + (z - z_0)^2 \right]^{\frac{1}{2}}. \tag{22}$$

The partial derivative of G has a negative sign because Kirchhoff's original formulation had the normal unit vector $\hat{\mathbf{u}}$ pointing in the $-z$ direction. We can safely ignore the $1/|\mathbf{r}|$ term in the bracket because the distance to the observation location from the lens $|\mathbf{r}|$ is much bigger than the wavelength ($|\mathbf{r}| \gg 1/k$, where $k = 2\pi/\lambda$). In this case, Eq. (21) can be simplified as

$$\left. \frac{\partial G}{\partial |\hat{\mathbf{u}}|} \right|_A = -\frac{\exp(ik|\mathbf{r}|)}{|\mathbf{r}|} ik \cos \alpha, \tag{23}$$

where $\hat{\mathbf{u}}$ is the unit vector of $\mathbf{r}_0$, and α is the angle between $\mathbf{r}$ and $\hat{\mathbf{u}}$. $\frac{\partial \mathbf{E}}{\partial |\hat{\mathbf{u}}|}$ in Eq. (18) can be expressed as

$$\left. \frac{\partial \mathbf{E}}{\partial |\hat{\mathbf{u}}|} \right|_A = \frac{\partial \mathbf{E}^{\mathrm{rs}}(r_0, \theta, \phi)}{\partial r_0}, \tag{24}$$

where r_0 is the magnitude of vector $\mathbf{r}_0$.

Substitution of Eqs. (23) and (24) into Eq. (18) gives a KVI-based solution for the propagation of the electric field toward the focal volume:

$$\mathbf{E}(\boldsymbol{\rho}) = \frac{-ik}{2\pi} \int \int_A \left(\mathbf{E}^{\mathrm{rs}}(r_0, \theta, \phi) \frac{\cos \alpha}{2} + \frac{\partial \mathbf{E}^{\mathrm{rs}}(r_0, \theta, \phi)}{\partial r_0} \frac{1}{2ik} \right) \times \frac{1}{|\mathbf{r}|} \exp(ik|\mathbf{r}|) \, \mathrm{d}A . \quad (25)$$

3. Huygens–Fresnel Principle—The HFP considers every point along a wavefront as a source of spherical wavelets. The electric field at any "downstream" location is given by the mutual interference of all wavelets arriving at that location. As dictated by Kirchhoff's boundary conditions, we know surfaces *B* and *C* have zero contribution to the electric field propagation. We can apply the HFP for surface *A* in Fig. 3 and write a scalar superposition integral as [64]

$$E(\boldsymbol{\rho}) = \int \int_A E^{\mathrm{rs}}(\theta, \phi) \, h(\mathbf{r}) \, \mathrm{d}A, \quad (26)$$

where $E^{\mathrm{rs}}(\theta, \phi)$ is a scalar electric field on the spherical reference surface and $h(\mathbf{r})$ is a weighting function:

$$h(\mathbf{r}) = \frac{-ik}{2\pi} \frac{\exp(ik|\mathbf{r}|)}{|\mathbf{r}|} K(\alpha), \quad (27)$$

where $K(\alpha)$ is known as the obliquity factor [16]. Equation (26) can be utilized to write three independent scalar equations that represent the Cartesian electric field components of $\mathbf{E}^{\mathrm{rs}}(\theta, \phi)$. Combining these scalar equations with Eq. (27), we can write

$$\mathbf{E}(\boldsymbol{\rho}) = \frac{-ik}{2\pi} \int \int_A \mathbf{E}^{\mathrm{rs}}(\theta, \phi) \, K(\alpha) \frac{1}{|\mathbf{r}|} \exp(ik|\mathbf{r}|) \, \mathrm{d}A . \quad (28)$$

The obliquity factor $K(\alpha)$ has several formulations [16,64,67–69]. The original selection of $\cos \alpha$ in Huygen's principle [64] is an excellent choice for forward propagation because $\cos \alpha$ is non-negative for $-\pi/2 \leq \alpha \leq \pi/2$, but beyond this range, $\cos \alpha$ is negative and thus specifies backward propagating contributions that do not exist in reality for freely propagating light (Fig. 4). Using the Fresnel–Kirchhoff diffraction formula, $K(\alpha)$ can be derived as $(1 + \cos \alpha)/2$ [16].

Even though this selection provides a non-zero contribution at $\alpha = \pi/2$, it does not provide a contribution in the backward direction. In practical focal field calculations, the choice of $\cos \alpha$ or $(1 + \cos \alpha)/2$ has no significant effect on the outcome in the limit that α is small. In what follows, we utilize $K(\alpha) = (1 + \cos \alpha)/2$ in Eq. (28). Using the HFP to compute the propagation of light from the lens to the focal volume, we can rewrite Eq. (28) as follows:

$$\mathbf{E}(\boldsymbol{\rho}) = \frac{-ik}{2\pi} \int \int_A \mathbf{E}^{\mathrm{rs}}(\theta, \phi) \frac{(1 + \cos \alpha)}{2} \frac{1}{|\mathbf{r}|} \exp(ik|\mathbf{r}|) \, \mathrm{d}A . \quad (29)$$

B. Comparison of DWI, KVI, and HFP Solution Integrals

The integral expressions obtained using these three methods have different forms. Table 1 highlights the differences in the integral expressions for the DWI, KVI, and HFP. The exponential factor in the DWI differs from the exponential factor in both the KVI and HFP. The DWI neither has an obliquity factor nor does it depend on the factor $1/|\mathbf{r}|$. Note that the DWI can describe the focal field with the same degree of accuracy as the KVI/HFP only when certain conditions are satisfied [70].

A mathematical difference between the KVI and HFP is that the KVI has the partial derivative of the field. Regardless of these differences, all three methods provide the same solution at the focal point because at that location, $|\mathbf{r}| = f_1$, $\psi_1 = \psi_2$, $\cos \alpha = 1$, and $\frac{\partial \mathbf{E}}{\partial r_0} = ik\,\mathbf{E}$. Below, we examine how the differences among these methods impact the focal field predictions at other locations.

1. Exponential Propagation Factor—The differences in the exponential propagation factors are difficult to appreciate since the form of the DWI in Eq. (16) is expressed in spherical coordinates, whereas the $|\mathbf{r}|$ term in the KVI and HFP is expressed in Cartesian coordinates. To understand the impact of the exponential factor, we compute each integral and observe the phase at the focal plane. We consider an x-polarized incident field, and substitute the form of $|\mathbf{r}|$ given in Eq. (22) into Eq. (25) or (29) and compare the result with the DWI expression. Figure 5(a) shows the phase of the dominant electric field component E_x using the KVI/HFP solution and the DWI solution. In the case of the KVI/HFP solution, the phase oscillation of E_x shows a gradual upward shift for locations away from the focal point. The greatest shift can be observed at the location farthest from the focal point. This is in contrast to the DWI prediction where the phase displays a steady oscillation without drift. The tiny spikes observed at the phase flipping locations in Fig. 5 are due to round-off and truncation errors during numerical integration.

This phase drift is significant within the focal plane only for locations away from the focal point. Its influence at other locations proximal to the focal point may be negligible. Nevertheless, it is instructive to analyze $|\mathbf{r}|$ in the exponent to understand its origin. Equation (22) can be rewritten as

$$|\mathbf{r}| = r_0 \left[1 - 2\left(\frac{x_0 x + y_0 y + z_0 z}{r_0^2} - \frac{x^2 + y^2 + z^2}{2 r_0^2} \right) \right]^{\frac{1}{2}} . \tag{30}$$

Application of the binomial approximation and replacement of r_0 by f_1 gives

$$|\mathbf{r}| = \left[f_1 - \frac{(x_0 x + y_0 y + z_0 z)}{f_1} + \frac{(x^2 + y^2 + z^2)}{2 f_1} \right] . \tag{31}$$

We now apply the Fraunhofer approximation, [16,53], which ignores the quadratic term in Eq. (31) when $2 f_1 \gg (x^2 + y^2 + z^2)$. This provides the following approximate form for $|\mathbf{r}|$:

$$|\mathbf{r}| = f_1 - \frac{(x_0 x + y_0 y + z_0 z)}{f_1}. \tag{32}$$

Utilizing spherical and cylindrical coordinates, we substitute $(x_0, y_0, z_0) = (f_1 \sin \theta \cos \phi, f_1 \sin \theta \sin \phi, -f_1 \cos \theta)$ and $(x, y, z) = (\rho \cos \varphi, \rho \sin \varphi, z)$, which allows us to write $ik|\mathbf{r}|$ in the exponent as

$$ik|\mathbf{r}| = ik\, f_1 + ikz \cos \theta - ik[\rho \sin \theta \cos (\phi - \varphi)]. \tag{33}$$

This argument is identical to that appearing in the exponent of the DWI in Eq. (16). The introduction of this simplified form of $|\mathbf{r}|$ in the exponent in Eqs. (25) or (29) diminishes the phase drift for locations away from the focal point on the focal plane as shown in Fig. 5(a), indicating that the quadratic terms in $\mathbf{r}$ are those that give rise to the phase drift away from the focal spot. Nevertheless, we will utilize the full expression for $|\mathbf{r}|$ as shown in the exponent of Eqs. (25) and (29) in the remainder of this tutorial.

2. Evaluation of the Partial Derivative in the KVI—The KVI contains the partial derivative of the field in Eq. (25). To compute this derivative, we need to determine the electric fields of two spherical reference surfaces with radii equal to $f_1 + \Delta r_0$ and $f_1 - \Delta r_0$. However, this computation can be simplified for certain wavefronts. Let us consider a monochromatic wavefront in the form of

$$A(r_0, \theta, \phi)r^p \exp(ikr_0) = \begin{cases} A(r_0, \theta, \phi) \exp(ikr_0) & p = 0 \\ A(r_0, \theta, \phi)\dfrac{1}{r} \exp(ikr_0) & p = -1, \end{cases} \tag{34}$$

where $p = 0$ represents plane waves and $p = -1$ represents diverging and converging beams. $A(\theta, \phi)r^p$ is the field amplitude at location (θ, ϕ). r is the distance $(r \gg 1/k)$ to the radiating point of a diverging beam or the point of convergence of a converging beam. The wave is assumed to propagate from left to right. The radiation point of the diverging beam is located on the left, and the point of convergence of the converging beam is located on the right.

When such a wavefront is incident upon the lens, we can write the partial derivative in Eq. (25) as a finite difference:

$$\begin{aligned} \frac{\partial \mathbf{E}^{\mathrm{rs}}(r_0, \theta, \phi)}{\partial r_0} &= \frac{1}{2\,\Delta r_0}\big[\mathbf{E}^{\mathrm{rs}}(r_0 + \Delta r_0, \theta, \phi) - \mathbf{E}^{\mathrm{rs}}(r_0 - \Delta r_0, \theta, \phi)\big] \\ &= \frac{1}{2\,\Delta r_0}\mathbf{E}^{\mathrm{rs}}(r_0, \theta, \phi)\big[\exp(ik\,\Delta r_0) - \exp(-ik\,\Delta r_0)\big] \\ &= ik\,\mathbf{E}^{\mathrm{rs}}(r_0, \theta, \phi)\left[\frac{\sin(k\,\Delta r_0)}{k\,\Delta r_0}\right] \\ &= ik\,\mathbf{E}^{\mathrm{rs}}(r_0, \theta, \phi)\mathrm{sinc}(k\,\Delta r_0), \end{aligned} \tag{35}$$

where Δr_0 is an infinitesimal distance along $\mathbf{r}_0$. When $\Delta r_0 \to 0$, the sin $c(k\Delta r_0)$ function approaches 1 [71]. This allows us to write Eq. (25) for the focused field as follows:

$$\mathbf{E}(\rho) = \frac{-ik}{2\pi} \int \int_A \mathbf{E}^{\mathrm{rs}}(\theta, \phi) \frac{(1 + \cos \alpha)}{2} \frac{1}{|\mathbf{r}|} \exp(ik|\mathbf{r}|) \, \mathrm{d}A \,. \tag{36}$$

We see that under these conditions, the solution of the KVI is identical to the integral expression obtained within the HFP [Eq. (29)].

3.   Multiplication Factors—The KVI and the HFP both contain an obliquity factor in the integrand, which is absent in the DWI. Figure 4 shows the obliquity factor variation with α. When α is very small and the lens has a long focal length, the effect of the obliquity factor is negligible. But if we consider a location far away from the focal point, α becomes larger and the results from the KVI/HFP will deviate from the DWI. Another difference we observe in Table 1 is the distance-dependent attenuation factor. The DWI uses $1/f$, while the KVI/HFP have a $1/|\mathbf{r}|$ term. To observe the combined effect of α and the attenuation factor, in Fig. 6, we compute the focal field amplitude along the x axis, y axis, and z axis using the solution from the KVI/HFP and the DWI for an incident plane wave. We also include the solution from the KVI/HFP with simplified $|\mathbf{r}|$ [Eq. (32)] in the exponent to avoid the impact from different exponential factors. The results show negligible differences between the different approaches.

C.   Numerical Evaluations

We have formulated the integral expressions using the DWI [Eq. (16)], KVI [Eq. (25)], and HFP [Eq. (29)] to represent the focal field. Here, we discuss how those integrals can be computed numerically.

1.   Debye–Wolf Integral—Solutions to the DWI [Eq. (16)] have been obtained for different illumination conditions after substitution with the following identity [53,55,57]:

$$\int_0^{2\pi} \exp(in\phi) \exp[\pm i\rho \cos(\phi - \varphi)] = 2\pi(\pm i)^n J_n(\rho) \exp(in\varphi) \,. \tag{37}$$

This substitution reduces the 2D integral to a 1D integral. For commonly used polarization states of the incident field, we can write the following 1D integrals [53,55,57]:

$$I_{00} = \int_0^{\theta_{\max}} A_0(\theta) \, a(\theta) \sin \theta (1 + \cos \theta) J_0(k\rho \sin \theta) \exp(i\psi) \, \mathrm{d}\theta, \tag{38}$$

$$I_{01} = \int_0^{\theta_{\max}} A_0(\theta) \, a(\theta) \sin^2 \theta J_1(k\rho \sin \theta) \exp(i\psi) \, \mathrm{d}\theta, \tag{39}$$

$$I_{02} = \int_0^{\theta_{\max}} A_0(\theta)\, a(\theta)\, \sin\theta (1 - \cos\theta) J_2(k\rho \sin\theta) \exp(i\psi)\, \mathrm{d}\theta, \tag{40}$$

where $A_0(\theta)$ is the beam amplitude given by Eq. (3) and $\psi = kz \cos\theta$. $A_0(\theta)$ can vary only with the polar angle θ. $a(\theta)$ is either Abbe's sine condition or Herschel's condition as given in Eq. (7).

We can solve these integrals numerically and express $\mathbf{E}(\rho)$ for different polarizations as linearly x polarized:

$$\mathbf{E}(\rho) = F\sqrt{\frac{n_{\mathrm{inc}}}{n_{\mathrm{m}}}} \begin{bmatrix} I_{00} + I_{02} \cos 2\varphi \\ I_{02} \sin 2\varphi \\ -2i\, I_{01} \cos \varphi \end{bmatrix}, \tag{41}$$

linearly y polarized:

$$\mathbf{E}(\rho) = F\sqrt{\frac{n_{\mathrm{inc}}}{n_{\mathrm{m}}}} \begin{bmatrix} I_{02} \sin 2\varphi \\ I_{00} - I_{02} \cos 2\varphi \\ -2i\, I_{01} \sin \varphi \end{bmatrix}, \tag{42}$$

linearly $+45°$ polarized:

$$\mathbf{E}(\rho) = \frac{F}{\sqrt{2}}\sqrt{\frac{n_{\mathrm{inc}}}{n_{\mathrm{m}}}} \begin{bmatrix} I_{00} + I_{02}(\cos 2\varphi + \sin 2\varphi) \\ I_{00} - I_{02}(\cos 2\varphi - \sin 2\varphi) \\ -2i\, I_{01}(\cos \varphi + \sin \varphi) \end{bmatrix}, \tag{43}$$

linearly $-45°$ polarized:

$$\mathbf{E}(\rho) = \frac{F}{\sqrt{2}}\sqrt{\frac{n_{\mathrm{inc}}}{n_{\mathrm{m}}}} \begin{bmatrix} I_{00} + I_{02}(\cos 2\varphi - \sin 2\varphi) \\ -I_{00} + I_{02}(\cos 2\varphi + \sin 2\varphi) \\ -2i\, I_{01}(\cos \varphi - \sin \varphi) \end{bmatrix}, \tag{44}$$

left circularly polarized:

$$\mathbf{E}(\rho) = \frac{F}{\sqrt{2}}\sqrt{\frac{n_{\mathrm{inc}}}{n_{\mathrm{m}}}} \begin{bmatrix} I_{00} + I_{02}(\cos 2\varphi + i \sin 2\varphi) \\ i\,I_{00} - i\,I_{02}(\cos 2\varphi + i \sin 2\varphi) \\ -2i\, I_{01}(\cos \varphi + i \sin \varphi) \end{bmatrix}, \tag{45}$$

and right circularly polarized:

$$\mathbf{E}(\rho) = \frac{F}{\sqrt{2}}\sqrt{\frac{n_{\mathrm{inc}}}{n_{\mathrm{m}}}} \begin{bmatrix} i\,I_{00} + i\,I_{02}(\cos 2\varphi - i \sin 2\varphi) \\ I_{00} - I_{02}(\cos 2\varphi - i \sin 2\varphi) \\ 2\,I_{01}(\cos \varphi - i \sin \varphi) \end{bmatrix}, \tag{46}$$

where

$$F = \frac{-ikf_1 \exp(ikf_1)}{2}. \tag{47}$$

2. KVI and HFP Integrals—To solve the area integral expressions for the KVI and HFP, we may express dA in either Cartesian ($dxdy$) or spherical coordinates ($\sin\theta \, d\phi d\theta$), before proceeding with the complicated double integration. Another approach that can be applied for this integral is to use a set of uniformly distributed radiating points on the spherical reference surface, so that surface element dA can be approximated as

$$dA \approx \frac{A}{N} = \frac{\int_0^{\theta_{max}} \int_0^{2\pi} f_1^2 \sin\theta \, d\phi \, d\theta}{N} = \frac{2\pi(1 - \cos\theta_{max})f_1^2}{N}, \tag{48}$$

where N is the number of radiating points on the reference surface and A represents the area of the spherical reference surface. This allows us to express the integral as a direct summation. The advantage of this integration approach is that all radiating points on the spherical reference surface are equally spaced, and any spatial variations of $\mathbf{E}^{rs}$ will be properly represented in the focal volume. If we consider traditional (θ, ϕ) sampling or $(\cos\theta, \phi)$ sampling, the spacing along ϕ will be different for different θ values, and the spatial variations of $\mathbf{E}^{rs}$ may not be properly represented in the focal volume. We adapt Koay's method [72] to uniformly sample the spherical reference surface. Note that (x, y) coordinates of the sampled points at the spherical reference surface should match the (x_∞, y_∞) coordinates in Eqs. (1)–(3). The best way to do this is to first sample the spherical reference surface and use the coordinates (x, y) of the surface to determine the coordinates (x_∞, y_∞) in Eqs. (1)–(3).

We use Eq. (48) to express the integral in Eqs. (25) and (29) as a summation. The solution obtained from the KVI [Eq. (25)] can now be written as

$$\mathbf{E}(\rho) = \frac{-ikf_1^2(1 - \cos\theta_{max})}{N} \times \sum_{j=1}^{N} \left[\mathbf{E}^{rs}(\theta, \phi)_j \frac{\cos\alpha_j}{2} + \frac{\partial \mathbf{E}^{rs}(r_0, \theta, \phi)_j}{\partial r_0} \frac{1}{2ik} \right] \times \frac{1}{|\mathbf{r}|_j} \tag{49}$$
$$\exp(ik|\mathbf{r}|_j),$$

where the partial derivative along $\mathbf{r}_0$ can be obtained by writing the central finite difference between $\Delta r_0^+ = f_1 + \Delta r_0$ and $\Delta r_0^- = f_1 - \Delta r_0$:

$$\frac{\partial \mathbf{E}^{rs}(r_0, \theta, \phi)}{\partial r_0} = \frac{1}{2\Delta r_0} \begin{bmatrix} E_x^{rs}(\Delta r_0^+, \theta, \phi) - E_x^{rs}(\Delta r_0^-, \theta, \phi) \\ E_y^{rs}(\Delta r_0^+, \theta, \phi) - E_y^{rs}(\Delta r_0^-, \theta, \phi) \\ E_z^{rs}(\Delta r_0^+, \theta, \phi) - E_z^{rs}(\Delta r_0^-, \theta, \phi) \end{bmatrix}, \tag{50}$$

where Δr_0 represents an infinitesimal distance along $\mathbf{r}_0$.

The solution obtained from the HFP [Eq. (29)] can be written as

$$\mathbf{E}(\boldsymbol{\rho}) = \frac{-ikf_1^2(1 - \cos\theta_{\max})}{N} \times \sum_{j=1}^{N} \mathbf{E}^{\mathrm{rs}}(\theta, \phi)_j \frac{(1 + \cos\alpha_j)}{2} \frac{1}{|\mathbf{r}|_j} \exp(ik|\mathbf{r}|_j), \qquad (51)$$

Where $\mathbf{E}^{\mathrm{rs}}(\theta, \phi)_j$ is the electric field wavelet (small section of a wave) on the jth location of the spherical surface. This summation is also known as an electric field superposition. The factor $(1 - \cos\theta_{\max})$ acts as a normalizing factor and attains the value of one when NA = 1. To obtain accurate results, it is important to select a sufficiently high value for N and perform a convergence test on the numerical integration scheme. A simple way to ensure this is to determine which of the Cartesian electric field amplitude components is the highest in the focal plane when using the DWI and increase the value used for N until the change in the value obtained for the integral becomes insignificant. In Fig. 7, we show the results obtained with the HFP solution to the diffraction integral. It shows the phase of each component.

D. Selection of Focused Beam Propagation Method

We have presented three integral methods that can be employed to model focused beam propagation in non-scattering media. We have provided a comparative analysis of these methods and shown how to compute them numerically. The DWI provides an efficient method for analyzing focal fields in homogeneous and stratified media [39,53,73,74] and is considered a good approximation to a well-posed boundary value problem [70]. However, any attempt to use the DWI in a scattering medium requires using either a representation of the scattering medium in k-space or an approach similar to that provided by Török and co-workers [46]. Representation of the scattering medium in k-space requires an evaluation of the effects of scattering and the propagation of the resulting k vector distribution before the application of the Fourier transform. To our knowledge, such a process has not been developed and applied for computing propagation in deterministic scattering media. The approach provided by Török's group [46] does not account for inter-particle scattering and is not easily applied to a medium with multiple scatterers. By contrast, solutions provided by the KVI and HFP are in a form that is readily applicable for computing both direct scattering and inter-particle scattering necessary for modeling various microscopy modalities. The KVI solution is computationally expensive because it requires the computation of electric field gradients at the lens. However, we have shown in Eqs. (34)–(36) that for converging, diverging, and plane wavefronts, this computation can be simplified, and that the simplified version is identical to the HFP. The HFP [Eq. (29)] is computationally efficient because it does not require the computation of electric field gradients. Our prior use of the HFP method has provided results that agree well with FDTD results [47].

5. FOCUSED BEAM PROPAGATION IN SCATTERING MEDIA

In this section, we outline an approach for describing the interaction of the focused beam wavefront with scatterers found in the medium between the focusing lens and the focal volume. While many other approaches have been discussed [41–46], each method has certain limitations. Here, we describe an approach grounded in the fundamentals of

scattering theory [14,15,17,47,48,75–77] and provide a comprehensive framework that can be applied to a variety of microscopy modalities under different illumination conditions.

A. Medium with a Single Scatterer

First, we discuss the modeling of focused beam propagation in the presence of a single scatterer within the medium. Second, we extend the approach for use in the case of multiple scatterers. Figure 8 depicts the graphical representation for the case of a single scatterer.

1.   Electric Field Components and Unit Vectors—Up to this point, we have represented the electric fields using their Cartesian components so that the total electric field can be determined through the vector addition of each Cartesian component. However, when performing scattering calculations, we must compute the incident electric field components that lie parallel and perpendicular to a scattering plane [15,17]. As shown in Fig. 8(a), the scattering plane contains the source, a scatterer, and an observation location. We can start with the parallel and perpendicular field components at the lens and apply the required coordinate transformations to obtain the incident field at the scatterer. It is also convenient to define unit vectors $\hat{\mathbf{m}}$ and $\hat{\mathbf{n}}$ of a local orthonormal coordinate system to track the parallel and perpendicular electric field components as well as unit vector $\hat{\mathbf{u}}$ that represents the propagation direction [47,75].

2.   Parallel and Perpendicular Components at the Lens—Consider a collimated beam incident upon the lens at location $L = (f_1 \sin \theta_l \cos \phi_l, f_1 \sin \theta_l \sin \phi_l, -f_1 \cos \theta_l)$. The first step is to consider the meridional plane as shown in Fig. 2 and compute the electric field components parallel and perpendicular to it, as follows:

$$\begin{bmatrix} E_\parallel^l(\theta_l, \phi_l) \\ E_\perp^l(\theta_l, \phi_l) \\ 0 \end{bmatrix} = \mathbb{L}^{-1} \cdot \mathbb{R} \cdot \mathbf{E}^{rs}(\theta_l, \phi_l), \tag{52}$$

where $\mathbb{L}^{-1}$ is equal to the transpose of $\mathbb{L}$ specified previously in Eq. (9). $E_\parallel^l(\theta_l, \phi_l)$ and $E_\perp^l(\theta_l, \phi_l)$ are electric field components parallel and perpendicular to the meridional plane, respectively, as shown in Fig. 8(a).

To track the parallel and perpendicular components, we can determine unit vectors $\hat{\mathbf{m}}^l = (\hat{m}_x^l, \hat{m}_y^l, \hat{m}_z^l)$ and $\hat{\mathbf{n}}^l = (\hat{n}_x^l, \hat{n}_y^l, \hat{n}_z^l)$ at location L for components $E_\parallel^l(\theta, \phi_l)$ and $E_\perp^l(\theta_l, \phi_l)$ in the following way:

$$\begin{bmatrix} \widehat{\mathbf{m}}^l \\ \widehat{\mathbf{n}}^l \end{bmatrix} = \begin{bmatrix} \cos \theta_l \cos \phi_l & \cos \theta_l \sin \phi_l & \sin \theta_l \\ -\sin \phi_l & \cos \phi_l & 0 \end{bmatrix}. \tag{53}$$

The unit vector that represents the propagation direction $\hat{\mathbf{u}}^l$ points towards the focal point F. It is given by $(-\sin \theta_l \cos \phi_l, -\sin \theta_l \sin \phi_l, \cos \theta_l)$.

3. Electric Field Propagation from Lens to Scatterer—Consider the placement of a scatterer at location $Q(\rho_q \cos \varphi_q, \rho_q \sin \varphi_q, z_q)$ as shown in Fig. 8(a). We aim to compute the incident electric field components $E_\parallel^{in}$ and $E_\perp^{in}$ at location Q. We start with $E_\parallel^l$ and $E_\perp^l$ and transform them to $E_\parallel^{lq}$ and $E_\perp^{lq}$ at location L. We then propagate the electric field towards location Q and apply another transformation to obtain $E_\parallel^{in}$ and $E_\perp^{in}$.

First, we find the direction of propagation of the wavelet $\hat{\mathbf{u}}^{lq}$ that points toward Q at location L:

$$\left[\hat{\mathbf{u}}^{lq}\right]^T = \begin{bmatrix} (\rho_q \cos \varphi_q - f_1 \sin \theta_i \cos \phi_i)/\left|\mathbf{r}^{lq}\right| \\ (\rho_q \sin \varphi_q - f_1 \sin \theta_i \sin \phi_i)/\left|\mathbf{r}^{lq}\right| \\ (z_q + f_1 \cos \theta_i)/\left|\mathbf{r}^{lq}\right| \end{bmatrix}, \tag{54}$$

and $\left|\mathbf{r}^{lq}\right|$ is the distance between L and Q. Second, we find a plane parallel to unit vector $\hat{\mathbf{u}}^{lq}$ because such a plane can be considered as the incident plane at Q. If we can find the angle pair that transforms LF to LQ, we can use it to map the meridional plane shown in Fig. 8(b) to a new plane parallel to $\hat{\mathbf{u}}^{lq}$ [78]. The transformation angle pair (ϕ_t and θ_t) can be computed as [79]

$$\phi_t = \arctan\left(\frac{\hat{\mathbf{n}}^l \cdot \hat{\mathbf{u}}^{lq}}{\hat{\mathbf{m}}^l \cdot \hat{\mathbf{u}}^{lq}}\right), \quad \theta_t = \arccos\left(\hat{\mathbf{u}}^l \cdot \hat{\mathbf{u}}^{lq}\right). \tag{55}$$

We can now write the relationship between $\left[E_\parallel^{lq}, E_\perp^{lq}\right]^T$ and $\left[E_\parallel^l, E_\perp^l\right]^T$ as

$$\begin{bmatrix} E_\parallel^{lq} \\ E_\perp^{lq} \end{bmatrix} = \begin{bmatrix} \cos \phi_t & \sin \phi_t \\ -\sin \phi_t & \cos \phi_t \end{bmatrix} \begin{bmatrix} E_\parallel^l \\ E_\perp^l \end{bmatrix}, \tag{56}$$

where $E_\parallel^{lq}$ is parallel and $E_\perp^{lq}$ is normal to the new plane that we have identified as the incident plane.

The unit vectors of the electric field components in Eq. (56) are shown in Fig. 8(c), and are given by

$$\begin{bmatrix} \hat{\mathbf{m}}^{lq} \\ \hat{\mathbf{n}}^{lq} \end{bmatrix} = [\mathbb{T}] \begin{bmatrix} \hat{\mathbf{m}}^l \\ \hat{\mathbf{n}}^l \end{bmatrix}, \tag{57}$$

where $\hat{\mathbf{m}}^{lq}$ and $\hat{\mathbf{n}}^{lq}$ are unit vectors of $E_\parallel^{lq}$ and $E_\perp^{lq}$, respectively, and the transformation matrix $\mathbb{T}$ is expressed as [78]

$$[\mathbb{T}] = \begin{bmatrix} \cos \theta_t \cos \phi_t & \cos \theta_t \sin \phi_t & -\sin \theta_t \\ -\sin \phi_t & \cos \phi_t & 0 \end{bmatrix}. \tag{58}$$

To account for the finite volume of the scatterer, we must consider separately each wavelet that reaches the scatterer. Let us consider the radiation from a single radiating point of the spherical reference surface that represents a partial field incident upon the scatterer at Q. We apply the solution provided by the HFP [Eq. (51)] to propagate a polarized wavelet from L towards Q and write the partial field $(E_\parallel^q, E_\perp^q)$ in Fig. 8(d) as

$$\begin{bmatrix} E_\parallel^q \\ E_\perp^q \end{bmatrix} = \frac{-ikf_1^2(1-\cos\theta_{max})}{N}\begin{bmatrix} E_\parallel^{lq}(\theta,\phi) \\ E_\perp^{lq}(\theta,\phi) \end{bmatrix} \times \left(\frac{1+\cos\theta_t}{2}\right)\frac{1}{|\mathbf{r}^{lq}|}\exp(ik|\mathbf{r}^{lq}|).$$
(59)

The local unit vectors at Q remain unchanged. $\left[\hat{\mathbf{m}}^q, \hat{\mathbf{n}}^q, \hat{\mathbf{u}}^q\right]^T$ is given by

$$\begin{bmatrix} \widehat{\mathbf{m}}^q \\ \widehat{\mathbf{n}}^q \\ \widehat{\mathbf{u}}^q \end{bmatrix} = \begin{bmatrix} \widehat{\mathbf{m}}^{lq} \\ \widehat{\mathbf{n}}^{lq} \\ \widehat{\mathbf{u}}^{lq} \end{bmatrix}.$$
(60)

We now know the partial field incident upon the scatterer at Q. However, its parallel and perpendicular components are given relative to the incident plane. Thus, the next step is to compute the parallel and perpendicular components relative to the scattering plane, as shown in Fig. 8(f). Similar to Eq. (55), we can compute the transformation angle pair (ϕ_s and θ_s) for this transformation as

$$\phi_s = \arctan\left(\frac{\widehat{\mathbf{n}}^q \cdot \widehat{\mathbf{u}}^s}{\widehat{\mathbf{m}}^q \cdot \widehat{\mathbf{u}}^s}\right), \quad \theta_s = \arccos\left(\widehat{\mathbf{u}}^q \cdot \widehat{\mathbf{u}}^s\right),$$
(61)

where the unit vector representing the propagation of the scattered field, $\hat{\mathbf{u}}^s$ in Fig. 8(g), can be determined as

$$\left[\widehat{\mathbf{u}}^s\right]^T = \begin{bmatrix} (\rho\cos\varphi - \rho_q\cos\varphi_q)/d \\ (\rho\sin\varphi - \rho_q\sin\varphi_q)/d \\ (z-z_q)/d \end{bmatrix},$$
(62)

and d is the distance from the scatterer to the observation location O at $\rho = (\rho\cos\varphi, \rho\sin\varphi, z)$.

We next transform the parallel and perpendicular components of E^q, which are defined relative to the incident plane, in terms of the parallel and perpendicular field components relative to the scattering plane, i.e., $\left[E_\parallel^{in}, E_\perp^{in}\right]^T$, as shown in Fig. 8(f). This transformation is given as

$$\begin{bmatrix} E_\parallel^{in} \\ E_\perp^{in} \end{bmatrix} = \begin{bmatrix} \cos\phi_s & \sin\phi_s \\ -\sin\phi_s & \cos\phi_s \end{bmatrix}\begin{bmatrix} E_\parallel^q \\ E_\perp^q \end{bmatrix} = [\mathbb{R}_2]\begin{bmatrix} E_\parallel^q \\ E_\perp^q \end{bmatrix},$$
(63)

where $\mathbb{R}_2$ represents a 2×2 transformation matrix.

The subsequent step is to obtain the unit vectors of $E_\parallel^{\text{in}}$ and $E_\perp^{\text{in}}$ as shown in Fig. 8(e). $\hat{\mathbf{m}}^{\text{in}}$ and $\hat{\mathbf{m}}^s$ lie in the same plane, and $\hat{\mathbf{n}}^{\text{in}}$ is collinear with $\hat{\mathbf{n}}^s$ [Fig. 8(g)]. When $|\cos \theta_s| = 1$, we can apply the azimuthal angle transformation given in Eq. (63) to compute unit vectors $\hat{\mathbf{m}}^s = \hat{\mathbf{m}}^{\text{in}} = (\hat{m}_x^q \cos \phi_s, \hat{m}_y^q \sin \phi_s, \hat{m}_z^q)$ and $\hat{\mathbf{n}}^s = \hat{\mathbf{n}}^{\text{in}} = (-\hat{n}_x^q \sin \phi_s, \hat{n}_y^q \cos \phi_s, \hat{n}_z^q)$. When $|\cos \theta_s| \neq 1$, we can write orthonormal unit vector relationships to determine $\hat{\mathbf{n}}^s$ and $\hat{\mathbf{n}}^{\text{in}}$ and then use that information to obtain $\hat{\mathbf{m}}^s$ and $\hat{\mathbf{m}}^{\text{in}}$[17]. This yields the following relations:

$$
\begin{cases}
\hat{\mathbf{n}}^s = \dfrac{\hat{\mathbf{u}}^{\text{in}} \times \hat{\mathbf{u}}^s}{\left|\hat{\mathbf{u}}^{\text{in}} \times \hat{\mathbf{u}}^s\right|}, \\
\hat{\mathbf{m}}^s = \hat{\mathbf{n}}^s \times \hat{\mathbf{u}}^s
\end{cases}
\begin{cases}
\hat{\mathbf{n}}^{\text{in}} = \dfrac{\hat{\mathbf{u}}^{\text{in}} \times \hat{\mathbf{u}}^s}{\left|\hat{\mathbf{u}}^{\text{in}} \times \hat{\mathbf{u}}^s\right|}. \\
\hat{\mathbf{m}}^{\text{in}} = \hat{\mathbf{n}}^{\text{in}} \times \hat{\mathbf{u}}^{\text{in}}
\end{cases}
\tag{64}
$$

4.   Computation of the Scattered Field—The rigorous computation of the scattered field is a tedious process and requires the evaluation of complex integral expressions [14,15,17] that follow from the solution for optical scattering produced by a dielectric particle. Once the incident electric field components are defined, we can consider the following simplified relationship to calculate the scattered far field [14,15,17,76]:

$$
\begin{aligned}
\begin{bmatrix} E_\parallel^s \\ E_\perp^s \end{bmatrix} &= \frac{i}{kd} \exp(ikd) \begin{bmatrix} S_2(\theta_s, \phi_s) & S_3(\theta_s, \phi_s) \\ S_4(\theta_s, \phi_s) & S_1(\theta_s, \phi_s) \end{bmatrix} \begin{bmatrix} E_\parallel^{\text{in}} \\ E_\perp^{\text{in}} \end{bmatrix} \\
&= \frac{i}{kd} \exp(ikd) \, [\mathbb{S}] \, [\mathbb{R}_2] \begin{bmatrix} E_\parallel^q \\ E_\perp^q \end{bmatrix},
\end{aligned}
\tag{65}
$$

where $[E_\parallel^s, E_\perp^s]^T$ are the parallel and perpendicular components of the scattered field, respectively, and $[E_\parallel^{\text{in}}, E_\perp^{\text{in}}]^T$ is given in Eq. (63). $S_1(\theta_s, \phi_s)$, $S_2(\theta_s, \phi_s)$, $S_3(\theta_s, \phi_s)$, and $S_4(\theta_s, \phi_s)$ are components of the scattering amplitude matrix $\mathbb{S}$[15,17].

To represent a matrix multiplication, we can place the common multiplier inside the scattering amplitude matrix and express the partial scattered field detected at the observation location for the jth wavelet as

$$
\begin{bmatrix} E_\parallel^s \\ E_\perp^s \end{bmatrix} = \left[\frac{i}{kd} \exp(ikd) \, \mathbb{S} \right] [\mathbb{R}_2] \begin{bmatrix} E_\parallel^q \\ E_\perp^q \end{bmatrix}_j .
\tag{66}
$$

To compute the full scattered field, we need to consider wavelets emanating from all locations on the spherical reference surface. However, the partial electric fields provided by Eq. (66) cannot be directly summed because the reference frames of parallel and perpendicular components are not identical across all the partial fields considered. Superposition can be performed only once all local parallel and perpendicular components

are converted to global Cartesian components. This conversion is accomplished using the following relationship:

$$\begin{bmatrix} E_x^s \\ E_y^s \\ E_z^s \end{bmatrix} = \begin{bmatrix} \widehat{m}_x^s \widehat{n}_x^s \\ \widehat{m}_y^s \widehat{n}_y^s \\ \widehat{m}_z^s \widehat{n}_z^s \end{bmatrix} \begin{bmatrix} E_\parallel^s \\ E_\perp^s \end{bmatrix} = \begin{bmatrix} \widehat{\mathbf{m}}^s \\ \widehat{\mathbf{n}}^s \end{bmatrix}^T \begin{bmatrix} E_\parallel^s \\ E_\perp^s \end{bmatrix}, \tag{67}$$

where $\hat{\mathbf{m}}^s = [\hat{m}_x^s, \hat{m}_y^s, \hat{m}_z^s]$ and $\hat{\mathbf{n}}^s = [\hat{n}_x^s, \hat{n}_y^s, \hat{n}_z^s]$ can be computed by the relations given in Eq (64).

To obtain the complete scattered field, we apply Eq. (59) for each wavelet that is oriented towards Q from the spherical reference surface and use it in Eqs. (66) and (67). The total scattered field at the observation location ρ due to a single scatterer can then be expressed as

$$\mathbf{E}^s(\rho) = \sum_{j=1}^{N} \begin{bmatrix} \widehat{\mathbf{m}}^s \\ \widehat{\mathbf{n}}^s \end{bmatrix}^T \left[\frac{i}{kd} \exp(ikd) \mathbb{S} \right] [\mathbb{R}_2] \begin{bmatrix} E_\parallel^q \\ E_\perp^q \end{bmatrix}_j$$

$$= \sum_{j=1}^{N} \mathbf{E}^s(\rho)\big|_j, \tag{68}$$

where $\mathbf{E}^s(\rho)\big|_j$ represents the partial scattered field detected at ρ in Cartesian form for the jth wavelet.

Note that Eq. (68) was derived for an observation location in the "far zone." Here, the far zone represents locations that satisfy $d \gg \max(\lambda, a, ka^2/2)$, where λ is wavelength, and a is the radius of the scatterer [17,76]. The distance between any point within the scatterer and the observation location should be greater than λ. For scatterers much smaller than the wavelength, the inequality $d \gg a$ defines the far-zone condition. For scatterers much larger than the wavelength, the inequality $d \gg ka^2/2$, which defines the Fraunhofer distance, determines the distance beyond which the far-zone expressions are valid [76].

5. Scattering Amplitude Matrix—We now take a closer look at the scattering amplitude matrix defined in Eq. (65). This matrix can be used for various scatterer shapes [48]. Here, we discuss how to obtain the scattering amplitude matrix components for spherical scatterers, which is a good approximation for the scattering objects relevant for optical microscopy of biological samples [50,80–82]. Rigorous computation of the scattered field for non-spherical scatterers is more complicated and beyond the scope of this tutorial.

For spherical scatterers, $S_3(\theta_s, \phi_s) = S_4(\theta_s, \phi_s) = 0$, and the azimuthal dependence of remaining $S_1(\theta_s, \phi_s), S_2(\theta_s, \phi_s)$ can be ignored. In this case, we may write the scattering amplitude matrix for spherical scatterers as

$$[\mathbb{S}] = \begin{bmatrix} S_2(\theta_s) & 0 \\ 0 & S_1(\theta_s) \end{bmatrix}, \tag{69}$$

where

$$S_1(\theta_s) = \sum_{n=1}^{\infty} \frac{(2n+1)}{n(n+1)}[a_n\pi_n(\cos\theta_s) + b_n\tau_n(\cos\theta_s)],$$

$$S_2(\theta_s) = \sum_{n=1}^{\infty} \frac{(2n+1)}{n(n+1)}[a_n\tau_n(\cos\theta_s) + b_n\pi_n(\cos\theta_s)],$$

(70)

where a_n and b_n are Mie scattering coefficients and $\pi_n(\cos\theta_s)$ and $\tau_n(\cos\theta_s)$ are Legendre functions [14,15].

6.   Application of Near-Field Lorenz–Mie Theory—The scattering amplitude matrix components $S_1(\theta_s)$ and $S_2(\theta_s)$ in the Mie solution are known as asymptotic scattering amplitudes at infinity. However, when the observation location or another spherical scatterer is located at a distance that does not satisfy the far-zone criteria specified above, we can apply results from near-field Lorenz–Mie theory [15,77,83] to obtain the scattered field in lieu of using $S_1(\theta_s)$ and $S_2(\theta_s)$. Near-field Lorenz–Mie theory contains distance-dependent components that are not fully transverse. The scattered field contains a radial component (E_r) in addition to polar (E_θ) and azimuthal (E_ϕ) components. However, we can ignore the effect of the radial component because it decays rapidly within an optical wavelength, and its effect on the overall result is negligible for well-separated scatterers. Assigning E_θ as the parallel component and E_ϕ as the perpendicular component, we can write a relationship similar to Eq. (65) as

$$\begin{bmatrix} E_\parallel^s \\ E_\perp^s \end{bmatrix} = \frac{i}{kd}\begin{bmatrix} E_\theta(\theta_s, kd) & 0 \\ 0 & E_\phi(\theta_s, kd) \end{bmatrix}[\mathbb{R}_2]\begin{bmatrix} E_\parallel^q \\ E_\perp^q \end{bmatrix}$$

$$= \left[\frac{i}{kd}\mathbb{E}(kd)\right][\mathbb{R}_2]\begin{bmatrix} E_\parallel^q \\ E_\perp^q \end{bmatrix},$$

(71)

where

$$E_\phi(\theta_s, d) = \sum_{n=1}^{\infty} \frac{(2n+1)}{n(n+1)}\left[i^n\xi'(kd)a_n\pi_n(\cos\theta_s) + i^{n+1}\xi(kd)b_n\tau_n(\cos\theta_s)\right],$$

$$E_\theta(\theta_s, d) = \sum_{n=1}^{\infty} \frac{(2n+1)}{n(n+1)}\left[i^n\xi'(kd)a_n\tau_n(\cos\theta_s) + i^{n+1}\xi(kd)b_n\pi_n(\cos\theta_s)\right].$$

(72)

Here, $\xi(kd)$ is the Riccati–Bessel function, and $\xi'(kd)$ is its derivative [14,15]. $\mathbb{E}(kd)$ represents a distance-dependent scattering matrix.

Note that Eq. (65) includes the phase term $\exp(ikd)$, which is not explicitly found in Eq. (71). The scattering amplitudes $S_1(\theta_s, \phi_s)$, $S_2(\theta_s, \phi_s)$, $S_3(\theta_s, \phi_s)$, and $S_4(\theta_s, \phi_s)$ in Eq. (65) are not distance-dependent functions and require a separate propagation phase to compute the scattered field at the observation location. Functions $\xi(kd)$ and $\xi'(kd)$ in Eq. (71), on the other hand, already include the propagation phase.

B. Medium with Multiple Scatterers

We now discuss how to extend the equations developed in Section 5.A to describe wave propagation in a medium containing multiple scatterers. When considering each scatterer independently, we can determine the scattered field due to primary scattering at the observation location. Additionally, we must consider the potential for multiple scattering, i.e., the possibility that the scattered field from one scatterer may act as an incident field on other scatterers and vice versa [Fig. 9(a)]. Fortunately, in many scenarios of practical interest, the scattered field undergoes considerable geometric attenuation before it is incident on another scatterer. Such an attenuated incident field produces an even weaker scattered field. Thus, the influence of this secondary scattered field on other scatterers, as shown in Fig. 9, is often negligibly small in many relevant cases.

To obtain an estimate of the magnitude of the secondary scattering effect, we considered the scenario shown in Fig. 9(a) and computed the primary and secondary scattering at ρ along the y axis for spherical scatterers. Figure 9(b) shows the primary and secondary scattering intensities for the arrangement in Fig. 9(a). In this scenario, we see that the secondary scattering intensities are, at most, two to three orders of magnitude smaller than the primary scattering intensities. Of course, these results do depend on the size and location of the secondary scatterer, but the scenario shown here is representative of the typical relative differences between primary and secondary scattering intensities.

In practice, the influence of tertiary or higher-order scattering can be safely ignored. We accordingly restrict our description to primary scattering and secondary scattering. With reference to Fig. 9(a), consider a field radiated from a dipole j that is incident on a scattering object Q. In the case of a nearby object R, following Eq. (68) derived for a single scatterer, we can write the scattered field observed at point ρ for multiple scatterers as

$$\mathbf{E}^s(\boldsymbol{\rho})\big|_j = \mathbf{E}^s_{\mathrm{pri}}(\boldsymbol{\rho})\big|_j + \mathbf{E}^s_{\mathrm{sec}}(\boldsymbol{\rho})\big|_j, \tag{73}$$

where the primary scattered field is

$$\mathbf{E}^s_{\mathrm{pri}}(\boldsymbol{\rho})\big|_j = \sum_{q=1}^{n_{\mathrm{scat}}} \begin{bmatrix} \widehat{\mathbf{m}}^s \\ \widehat{\mathbf{n}}^s \end{bmatrix}_q^T \left[\frac{i}{kd_q} \exp(ikd_q)\mathbb{S}_q \right] [\mathbb{R}_{2q\rho}] \begin{bmatrix} E_\parallel^q \\ E_\perp^q \end{bmatrix}_j \tag{74}$$

and the secondary scattering field is

$$\mathbf{E}^s_{\mathrm{sec}}(\boldsymbol{\rho})\big|_j = \sum_{q=1}^{n_{\mathrm{scat}}} \left\{ \sum_{r(\neq q)=1}^{n_{\mathrm{sat}}} \begin{bmatrix} \widehat{\mathbf{m}}^s \\ \widehat{\mathbf{n}}^s \end{bmatrix}_r^T \left[\frac{i}{kd_r} \exp(ikd_r)\mathbb{S}_r \right] [\mathbb{R}_{2r\rho}] \right.$$

$$\left. \times \left(\left[\frac{i}{kd_{qr}} \exp(ikd_{qr})\mathbb{S}_q \right] [\mathbb{R}_{2qr}] \begin{bmatrix} E_\parallel^q \\ E_\perp^q \end{bmatrix}_j \right) \right\}. \tag{75}$$

Here, n_{scat} is the number of scatterers in the media, and $\mathbb{S}_q$ and $\mathbb{S}_r$ are the scattering amplitude matrices for the Qth and Rth scatterers, respectively. $\mathbb{R}_{2q\rho}$ is a 2×2 transformation matrix at the Qth scatterer with an observation location at ρ. $\mathbb{R}_{2r\rho}$ is a 2×2 transformation matrix at the Rth scatterer with an observation location at ρ. $\mathbb{R}_{2qr}$ is a 2×2 transformation matrix at the Qth scatterer with an observation location at the Rth scatterer [Fig. 9(a)]. $[\hat{\mathbf{m}}, \hat{\mathbf{n}}]_q^T$ and $[\hat{\mathbf{m}}, \hat{\mathbf{n}}]_r^T$ transform parallel and perpendicular components to Cartesian components, and subscripts q and r represent Qth and Rth scatterers, respectively.

When we consider all locations of the spherical reference surface, the total scattered field at ρ is given by

$$\mathbf{E}^s(\boldsymbol{\rho}) = \sum_{j=1}^{N} \left[\mathbf{E}_{\text{pri}}^s(\boldsymbol{\rho})_j + \mathbf{E}_{\text{sec}}^s(\boldsymbol{\rho})_j \right]. \tag{76}$$

When the near-field Lorenz–Mie theory is considered, the $\exp(ikd)\mathbb{S}$ matrix in Eqs. (74) and (75) and the other primary and secondary scattering expressions in Part II [51] should be replaced with $\mathbb{E}(kd)$ as shown in Eq. (71).

Figure 10(a) shows the computed scattered electric field based on Eq. (76). Two scatterers are placed prior to the focal plane, and three scatterer diameters are considered: 1 μm, 2.5 μm and 5 μm. The results are in excellent agreement with the FDTD results given in Fig. 10(b). We note that the results obtained from Eq. (76) may lack accuracy in the immediate near field of the scatterers because of the missing radial component. On the other hand, the FDTD results may be affected by the focused beam implementation technique, discretization errors, and unavoidable reflections from the perfectly matched layer (PML) [27,28]. The results obtained in Eq. (76) and FDTD simulations near the focal plane are compared numerically in [47].

When scatterers are involved, a detector at ρ captures the total electric field $\mathbf{E}^{\text{tot}}(\rho)$ representing the superposition of both incident $\mathbf{E}(\rho)$ and scattered $\mathbf{E}^s(\rho)$ fields [14,15,17]:

$$\mathbf{E}^{\text{tot}}(\boldsymbol{\rho}) = \mathbf{E}(\boldsymbol{\rho}) + \mathbf{E}^s(\boldsymbol{\rho}). \tag{77}$$

$\mathbf{E}(\rho)$ in Eq. (77) is provided by Eq. (49) or Eq. (51). The corresponding intensity of the field at the location of a nonlinearly polarizable object is proportional to $|E_x|^2 + |E_y|^2 + |E_z|^2$, where E_x, E_y, and E_z are Cartesian components of $\mathbf{E}^{\text{tot}}(\rho)$. It is the computation of the total electric field and corresponding intensities within the focal volume that provides the critical input to determine the generation of optical signals within the focal volume considered in Part II of this tutorial.

6. CONCLUSION AND FURTHER READING

We have provided a framework that utilizes classical analytical electromagnetic field propagation methods to comprehensively model optical microscopy in scattering samples with fixed scatterer configurations. The equations used in the tutorial for propagating light in non-scattering media originate from the vectorial and scalar theory of diffraction and focusing. Their foundation and application can be found in [15,39,40,53,54,57,64].

We have limited our scope to spherical scatterers, which are generally considered to provide a good approximation to the scattering objects relevant for optical microscopy of biological samples. Rigorous modeling and computation of the scattered field for non-spherical scatterers is more complicated and is treated in [48,84].

We have treated both primary and secondary scattering. The inclusion of secondary scattering increases the computational time exponentially. Secondary scattering becomes important once scatterers are larger than three to four times the wavelength and when they are located very close to each other. In other cases, the effect of secondary scattering on the final result is rather low and may be ignored. In cases where the scatterers are smaller than the wavelength with the neighboring scatterers located in the far zone, secondary scattering can be safely neglected.

In Part II of this tutorial [51], we consider focal field distributions in the presence of scatterers, signal generation, radiation, and far-field detection. We also provide a case study that includes two-photon and SHG microscopy.

Data availability.

Data underlying the results presented in this paper are not publicly available at this time but may be obtained from the authors upon reasonable request.
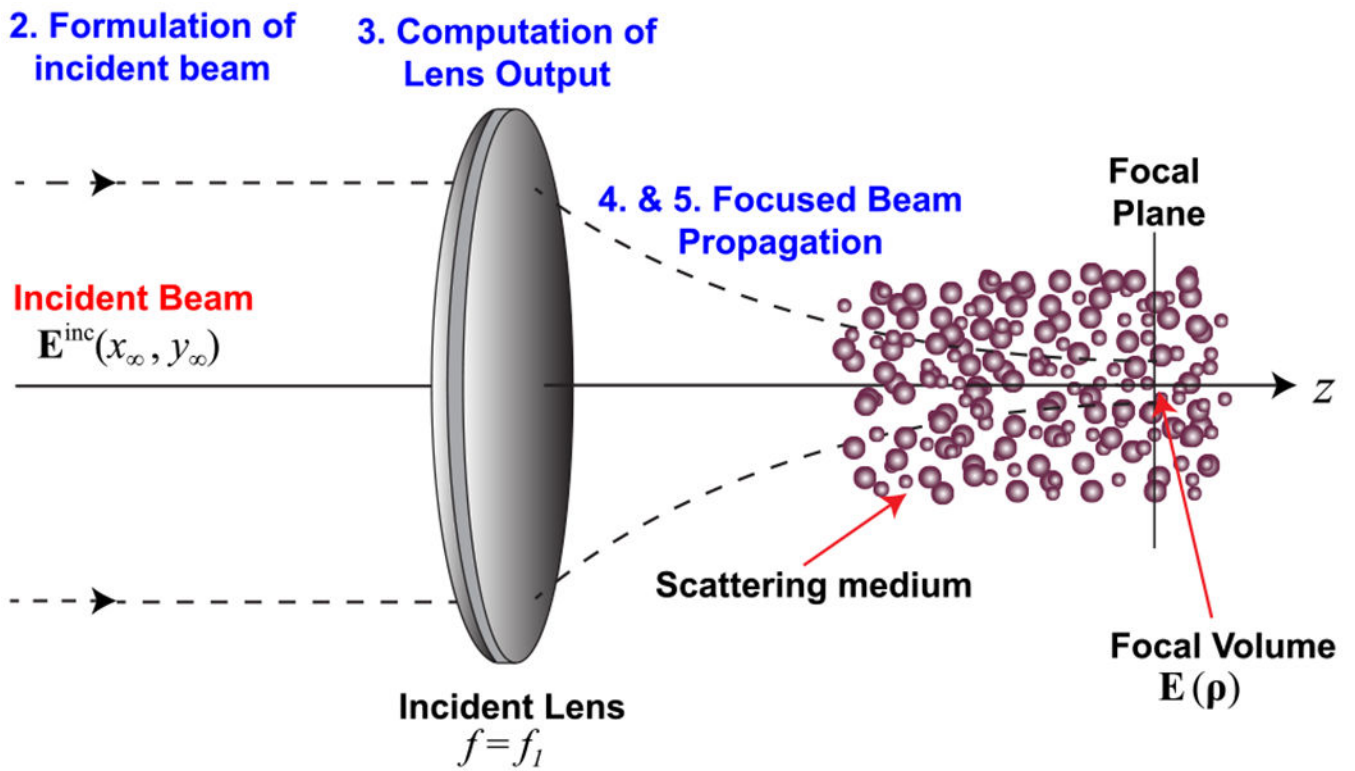
REFERENCES

1. Wilt BA, Burns LD, Ho ETW, Ghosh KK, Mukamel EA, and Schnitzer MJ, "Advances in light microscopy for neuroscience," Annu. Rev. Neurosci 32, 435–506 (2009). [PubMed: 19555292]
2. Kanchanawong P and Waterman CM, "Advances in light-based imaging of three-dimensional cellular ultrastructure," Curr. Opin. Cell Biol 24, 125–133 (2012). [PubMed: 22209239]
3. Zhang C, Zhang D, and Cheng J-X, "Coherent Raman scattering microscopy in biology and medicine," Annu. Rev. Biomed. Eng 17, 415–445 (2015). [PubMed: 26514285]
4. Ntziachristos V., "Going deeper than microscopy: the optical imaging frontier in biology," Nat. Methods 7, 603–614 (2010). [PubMed: 20676081]

5. Wang K, Horton NG, and Xu C, "Going deep: brain imaging with multi-photon microscopy," Opt. Photon. News 24(11), 32–39 (2013).

6. Vellekoop IM and Mosk AP, "Focusing coherent light through opaque strongly scattering media," Opt. Lett 32, 2309–2311 (2007). [PubMed: 17700768]

7. Sinefeld D, Paudel HP, Ouzounov DG, Bifano TG, and Xu C, "Adaptive optics in multiphoton microscopy: comparison of two, three and four photon fluorescence," Opt. Express 23, 31472–31483 (2015). [PubMed: 26698772]

8. Hampson KM, Turcotte R, Miller DT, Kurokawa K, Males JR, Ji N, and Booth MJ, "Adaptive optics for high-resolution imaging," Nat Rev Methods Primers. 1, 68 (2021). [PubMed: 35252878]

9. Katz O, Small E, Guan Y, and Silberberg Y, "Noninvasive nonlinear focusing and imaging through strongly scattering turbid layers," Optica 1, 170–174 (2014).

10. Tao X, Lam T, Zhu B, Li Q, Reinig MR, and Kubby J, "Three-dimensional focusing through scattering media using conjugate adaptive optics with remote focusing (CAORF)," Opt. Express 25, 10368–10383 (2017) [PubMed: 28468409]

11. Booth MJ, "Adaptive optical microscopy: the ongoing quest for a perfect image," Light Sci. Appl 3, e165 (2014).

12. Kubby J, Gigan, and Cui M, eds., Wavefront Shaping for Biomedical Imaging (Cambridge, 2019).

13. Débarre D, Booth MJ, and Wilson T, "Image based adaptive optics through optimisation of low spatial frequencies," Opt. Express 15, 8176–8190 (2007). [PubMed: 19547145]

14. van de Hulst HC, Light Scattering by Small Particles (Wiley, 1957).

15. Bohren CF and Huffman DR, Absorption and Scattering of Light by Small Particles (Wiley, 1983).

16. Born M and Wolf E, Principles of Optics, 7th ed. (Cambridge University, 1999).

17. Kristensson G., Scattering of Electromagnetic Waves by Obstacles (SciTech, 2016).

18. Gan X and Gu M, "Spatial distribution of single-photon and two-photon fluorescence light in scattering media: Monte Carlo simulation," Appl. Opt 39, 1575–1579 (2000). [PubMed: 18345054]

19. Hayakawa CK, Venugopalan V, Krishnamachari VV, and Potma EO, "Amplitude and phase of tightly focused laser beams in turbid media," Phys. Rev. Lett 103, 043903 (2009). [PubMed: 19659354]

20. Hayakawa CK, Potma EO, and Venugopalan V, "Electric field Monte Carlo simulations of focal field distributions produced by tightly focused laser beams in tissues," Biomed. Opt. Express 2, 278–299 (2011). [PubMed: 21339874]

21. Hokr BH, Bixler JN, Elpers G, Zollars B, Thomas RJ, Yakovlev VV, and Scully MO, "Modeling focusing Gaussian beams in a turbid medium with Monte Carlo simulations," Opt. Express 23, 8699–8705 (2015). [PubMed: 25968708]

22. Glaser AK, Chen Y, and Liu JTC, "Fractal propagation method enables realistic optical microscopy simulations in biological tissues," Optica 3, 861–869 (2016). [PubMed: 28983499]

23. Gu M, Fan X, and Sheppard C, "Three-dimensional coherent transfer functions in fiber-optical confocal scanning microscopes," J. Opt. Soc. Am. A 8, 1019–1025 (1991).

24. Chen M, Ren D, Liu H-Y, Chowdhury S, and Waller L, "Multi-layer Born multiple-scattering model for 3D phase microscopy," Optica 7, 394–403 (2020).

25. Su R, Coupland J, Sheppard C, and Leach R, "Scattering and three-dimensional imaging in surface topography measuring interference microscopy," J. Opt. Soc. Am. A 38, A27–A42 (2021).

26. Török P, Munro PRT, and Kriezis EE, "High numerical aperture vectorial imaging in coherent optical microscopes," Opt. Express 16, 507–523 (2008). [PubMed: 18542126]

27. Starosta MS, Dunn AK, and Thomas RJ, "Three-dimensional computation of focused beam propagation through multiple biological cells," Opt. Express 17, 12455–12469 (2009). [PubMed: 19654647]

28. Çapoglu IR, Rogers JD, Taflove A, and Backman V, "The microscope in a computer: image synthesis from three-dimensional full-vector solutions of Maxwell's equations at the nanometer scale," Prog. Opt 57, 1–91 (2012).

29. Tseng SH, "2-D PSTD Simulation of focusing monochromatic light through a macroscopic scattering medium via optical phase conjugation," Biomed. Opt. Express 6, 815–826 (2015). [PubMed: 25798306]

30. Zhang D, Capoglu I, Li Y, Cherkezyan L, Chandler J, Spicer G, Subramanian H, Taflove A, and Backman V, "Finite-difference time-domain-based optical microscopy simulation of dispersive media facilitates the development of optical imaging techniques," J. Biomed. Opt 21, 065004 (2016). [PubMed: 27283256]

31. Çapoglu IR, Taflove A, Backman V, Capoglu IR, Taflove A, and Backman V, "Generation of an incident focused light pulse in FDTD," Opt. Express 16, 19208–19220 (2008). [PubMed: 19582013]

32. Munro PR, Engelke D, and Sampson DD, "A compact source condition for modelling focused fields using the pseudospectral time-domain method," Opt. Express 22, 5599–5613 (2014). [PubMed: 24663901]

33. Wu Z, Han Y, Wang J, and Cui Z, "Generation of Bessel beam sources in FDTD," Opt. Express 26, 28727–28737 (2018). [PubMed: 30470045]

34. Mazzolani A, Macdonald CM, and Munro PRT, "Application of a Taylor series approximation to the Debye-Wolf integral in time-domain numerical electromagnetic simulations," J. Opt. Soc. Am. A 39, 927–935 (2022).

35. McCoy DE, Shneidman AV, Davis AL, and Aizenberg J, "Finite-difference time-domain (FDTD) optical simulations: a primer for the life sciences and bio-inspired engineering," Micron 151, 103160 (2021). [PubMed: 34678583]

36. Török P, Munro PR, and Kriezis EE, "Rigorous near-to far-field transformation for vectorial diffraction calculations and its numerical implementation," J. Opt. Soc. Am. A 23, 713–722 (2006).

37. He Y and Guo Q, "Accuracy improvement of near-to-far-field transformation in FDTD calculation," in 11th European Conference on Antennas and Propagation (EUCAP) (2017), pp. 1106–1108.

38. van de Nes AS, Billy L, Pereira SF, and Braat JJM, "Calculation of the vectorial field distribution in a stratified focal region of a high numerical aperture imaging system," Opt. Express 12, 1281–1293 (2004). [PubMed: 19474948]

39. Munro PR, "Tool for simulating the focusing of arbitrary vector beams in free-space and stratified media," J. Biomed. Opt 23, 090801 (2018).

40. Foreman MR and Török P, "Computational methods in vectorial imaging," J. Mod. Opt 58, 339–364 (2011).

41. Barton JP, Alexander DR, and Schaub SA, "Internal and near-surface electromagnetic fields for a spherical particle irradiated by a focused laser beam," J. Appl. Phys 64, 1632–1639 (1988).

42. van de Nes AS and Torok P, "Rigorous analysis of spheres in Gauss-Laguerre beams," Opt. Express 15, 13360–13374 (2007). [PubMed: 19550606]

43. Hoang TX, Chen X, and Sheppard CJR, "Interpretation of the scattering mechanism for particles in a focused beam," Phys. Rev. A 86, 033817 (2012).

44. Bareil PB and Sheng Y, "Modeling highly focused laser beam in optical tweezers with the vector Gaussian beam in the T-matrix method," J. Opt. Soc. Am. A 30, 1–6 (2013).

45. Kiselev AD and Plutenko DO, "Mie scattering of Laguerre-Gaussian beams: photonic nanojets and near-field optical vortices," Phys. Rev. A 89, 043803 (2014).

46. Török P, Higdon PD, Juškaitis R, and Wilson T, "Optimising the image contrast of conventional and confocal optical microscopes imaging finite sized spherical gold scatterers," Opt. Commun 155, 335–341 (1998).

47. Ranasinghesagara JC, Hayakawa CK, Davis MA, Dunn AK, Potma EO, and Venugopalan V, "Rapid computation of the amplitude and phase of tightly focused optical fields distorted by scattering particles," J. Opt. Soc. Am. A 31, 1520–1530 (2014).

48. Mishchenko MI, Davis LD, and Lacis AA, Multiple Scattering of Light by Particles (Cambridge University, 2006).

49. Mackowski DW and Mishchenko MI, "A multiple sphere T-matrix Fortran code for use on parallel computer clusters," J. Quant. Spectrosc. Radiat. Transfer 112, 2182–2192 (2011).

50. Ranasinghesagara JC, De Vito G, Piazza V, Potma EO, and Venugopalan V, "Effect of scattering on coherent anti-Stokes Raman scattering (CARS) signals," Opt. Express 25, 8638–8652 (2017). [PubMed: 28437941]

51. Ranasinghesagara JC, Potma EO, and Venugopalan V, "Modeling nonlinear optical microscopy in scattering media, part II. Radiation from focal volume to far-field: tutorial," J. Opt. Soc. Am. A 40, 883–897 (2023).

52. Hecht E., Optics, 4th ed. (Addison-Wesley, 2001).

53. Braat J and Török P, Imaging Optics (Cambridge University, 2019).

54. Török P, Higdon PD, and Wilson T, "On the general properties of polarised light conventional and confocal microscopes," Opt. Commun 148, 300–315 (1998).

55. Novotny L and Hecht B, Principles of Nano-Optics (Cambridge University, 2006).

56. Azzam R and Bashra N, Ellipsometry and Polarized Light (Elsevier, 1987).

57. Richards B and Wolf E, "Electromagnetic diffraction in optical systems. II. Structure of the image field in an aplanatic system," Proc. Royal Soc. London A 253, 358–379 (1959).

58. Kim J, Wang Y, and Zhang X, "Calculation of vectorial diffraction in optical systems," J. Opt. Soc. Am. A 35, 526–535 (2018).

59. Stamnes JJ, Waves in Focal Regions: Propagation, Diffraction and Focusing of Light, Sound and Water Waves (Hilger, 1986).

60. Hopkins HH, "Herschel's condition," Proc. Phys. Soc 58, 100–105 (1946).

61. Abbe E., "On the estimation of aperture in the microscope," J. R. Microsc. Soc 1, 388–423 (1881).

62. Ignatowsky VS, "Diffraction by a lens of arbitrary aperture," Trans. Opt. Inst. Petrograd 1, 1–36 (1919).

63. Luneburg RK, Mathematical Theory of Optics (University of California, 1966).

64. Goodman JW, Introduction to Fourier Optics (McGraw-Hill, 1968).

65. Stratton JA and Chu LJ, "Diffraction theory of electromagnetic waves," Phys. Rev 56, 99–107 (1939).

66. Török P, "Focusing of electromagnetic waves through a dielectric interface by lenses of finite Fresnel number," J. Opt. Soc. Am. A 15, 3009–3015 (2006).

67. Piaggio H, "The mathematical theory of Huygens' principle," Nature 145, 531–532 (1940)

68. Miller DAB, "Huygen's wave propagation principle corrected," Opt. Lett 16, 1370–1372 (1991). [PubMed: 19776972]

69. Depasse F, Paesler MA, Courjon D, and Vigoureux JM, "Huygens-Fresnel principle in the near field," Opt. Lett 20, 234–236 (1995). [PubMed: 19859145]

70. Wolf E and Li Y, "Conditions for the validity of the Debye integral representation of focused fields," Opt. Commun 39, 205–210 (1981).

71. Olver FWJ, Lozier DW, Boisvert RF, and Clark CW, eds., NIST Handbook of Mathematical Functions (Cambridge University, 2010).

72. Koay CG, "A simple scheme for generating nearly uniform distribution of antipodally symmetric points on the unit sphere," J. Comput. Sci 2, 377–381 (2011). [PubMed: 22125587]

73. O'Neil M, "A generalized Debye source approach to electromagnetic scattering in layered media," J. Math. Phys 55, 012901 (2014).

74. Leutenegger M, Rao R, Leitgeb RA, and Lasser T, "Fast focus field calculations," Opt. Express 14, 11277–11291 (2006). [PubMed: 19529543]

75. Xu M, "Electric field Monte Carlo simulation of polarized light propagation in turbid media," Opt. Express 12, 6530–6539 (2004). [PubMed: 19488304]

76. Mishchenko MI, "Far-field approximation in electromagnetic scattering," J. Quant. Spectrosc. Radiat. Transfer 100, 268–276 (2006).

77. Stratton JA, Electromagnetic Theory (McGraw-Hill, 1941).

78. Arfken GB and Weber HJ, Mathematical Methods for Physicists, 7th ed. (Academic, 2012).

79. Boyd S and Vandenberghe L, Introduction to Linear Algebra: Vectors, Matrices and Least Squares (Cambridge University, 2018).

80. Smith ZJ and Berger AJ, "Validation of an integrated Ramanand angular-scattering microscopy system on heterogeneous bead mixtures and single human immune cells," Appl. Opt 48, D109–D120 (2009). [PubMed: 19340098]

81. Xu M, Wu TT, and Qu JY, "Unified Mie and fractal scattering by cells and experimental study on application in optical characterization of cellular and subcellular structures," J. Biomed. Opt 13, 024015 (2014).

82. Lesina AC, van der Kolk J, Berini P, and Ramunno L, "Computational electrodynamics - a powerful tool for nanophotonics and microscopy," MRS Adv. 3, 753–760 (2018).

83. Slimani F, Grehan G, Gouesbet G, and Allano D, "Near-field Lorenz-Mie theory and its application to microholography," Appl. Opt 23, 4140–4148 (1984). [PubMed: 18213288]

84. Mishchenko MI, "Calculation of the amplitude matrix for a non-spherical particle in a fixed orientation," Appl. Opt 39, 1026–1031 (2000). [PubMed: 18337981]

Fig. 1.

Excitation part of a basic microscopy system. Incident beam $\mathbf{E}^{inc}(x_\infty, y_\infty)$ is considered as a collimated beam. The number in front of the process indicates the related sections in this tutorial.
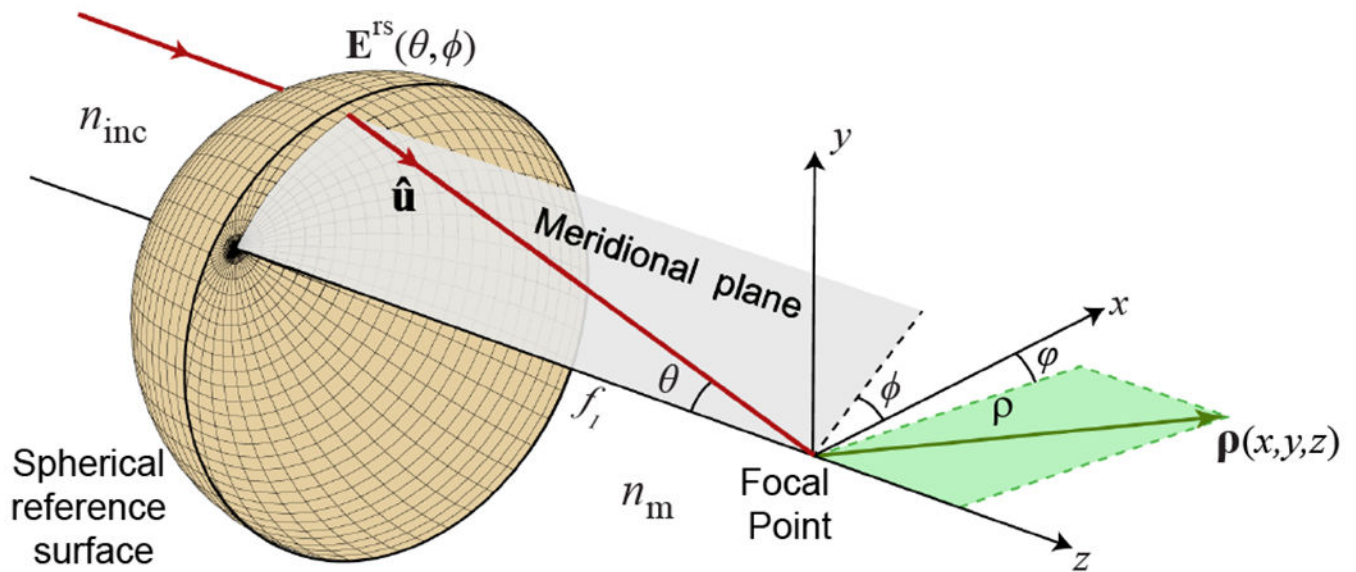
Fig. 2.
Depiction of the spherical reference surface and coordinate system. The origin is placed at the focal point. We consider a refracted ray that emanates from the source and lies on a meridional plane that contains both the optical axis (z axis) and refracted ray under consideration. This ray points toward the focal point and is oriented at a polar angle θ relative to the $-z$ axis and an azimuthal angle ϕ relative to the $+x$ axis on the plane perpendicular to the z axis.
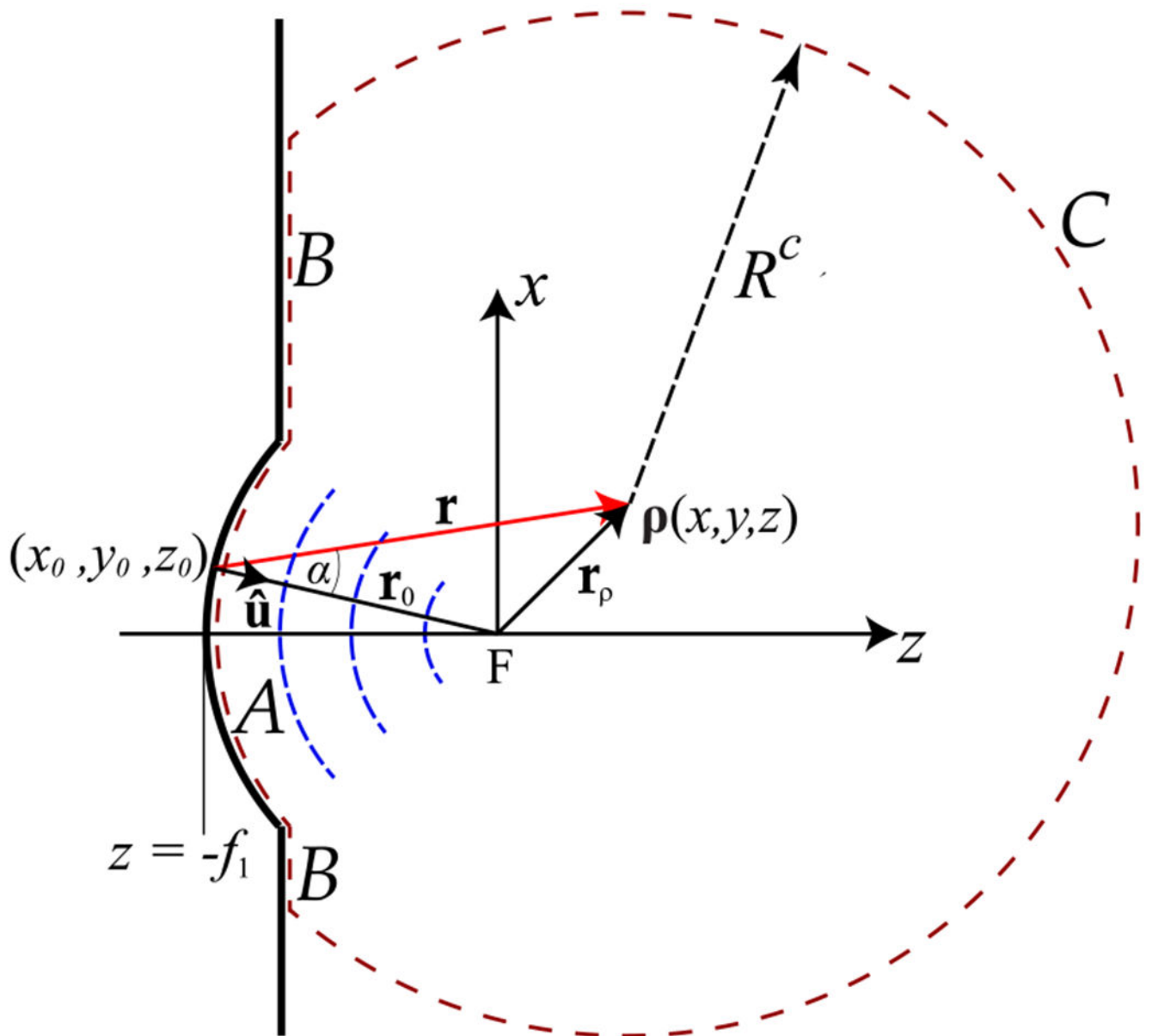
Fig. 3.
Diffraction by the spherical reference surface aperture. *A* is the spherical reference surface, and *B* is a plane outside of the spherical reference surface whose orientation is perpendicular to the *z* axis. *C* is a large spherical surface centered around the observation point $\rho(x, y, z)$. (x_0, y_0, z_0) represents any point on the reference surface. *F* is the focal point at the origin. The origin of the Cartesian coordinate system lies at focal point *F*.
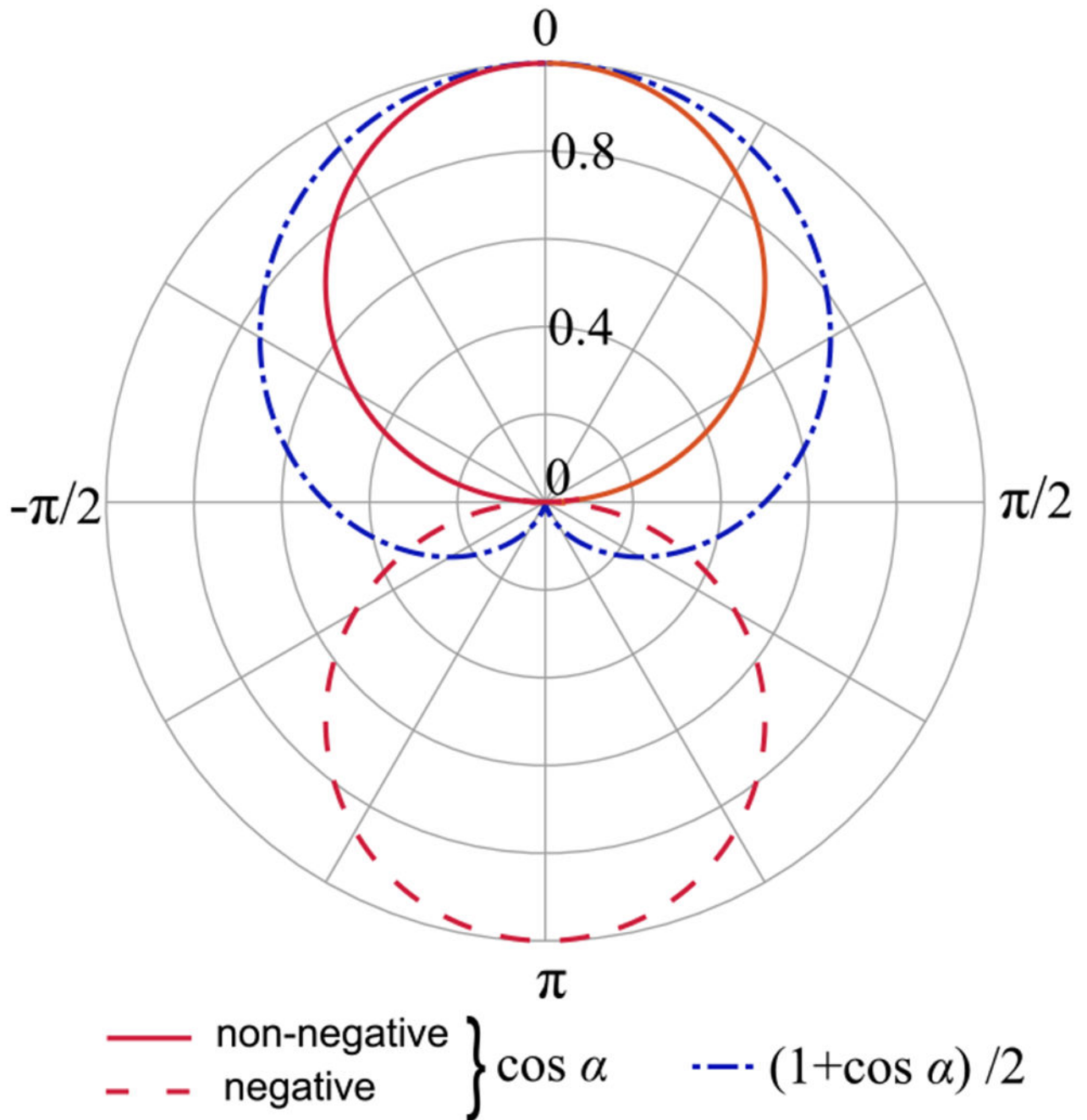
Fig. 4.
Polar plots of obliquity factors $K(\alpha) = \cos \alpha$ [64] and $K(\alpha) = (1 + \cos \alpha)/2$ [16]. While $(1 + \cos \alpha)/2$ is non-negative for the whole α range, $\cos \alpha$ is non-negative for only $-\pi/2 \leq \alpha \leq \pi/2$.
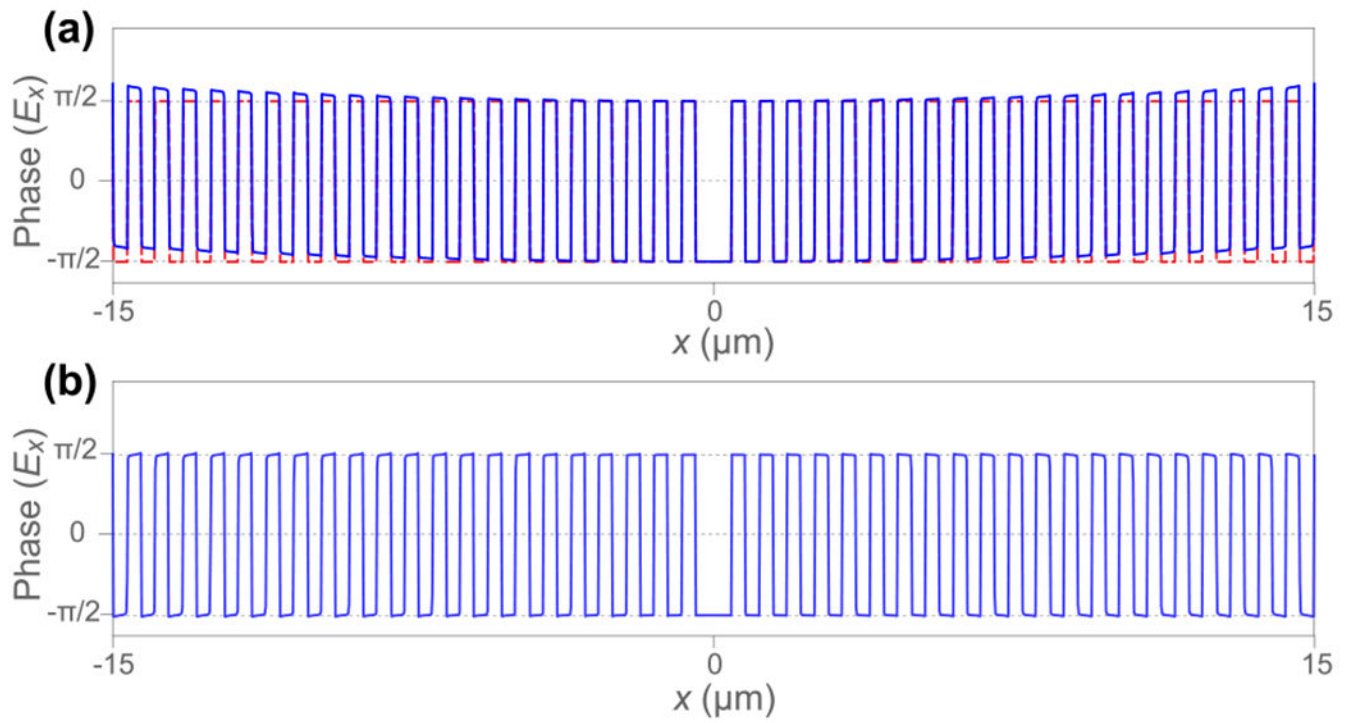
Fig. 5.
Dependency of $|\mathbf{r}|$ on the exponent. Phase of dominant component E_x at the focal plane for x-polarized incidence. (a) Results obtained using the KVI/HFP solution with expression for $|\mathbf{r}|$ stated in Eq. (22) (solid blue) and DWI solution (dashed red). (b) Results obtained using KVI/HFP solution with simplified $|\mathbf{r}|$ without quadratic terms in Eq. (32) (solid blue). Incident wavelength is 0.8μm and NA = 0.866; medium refractive index is 1.333.
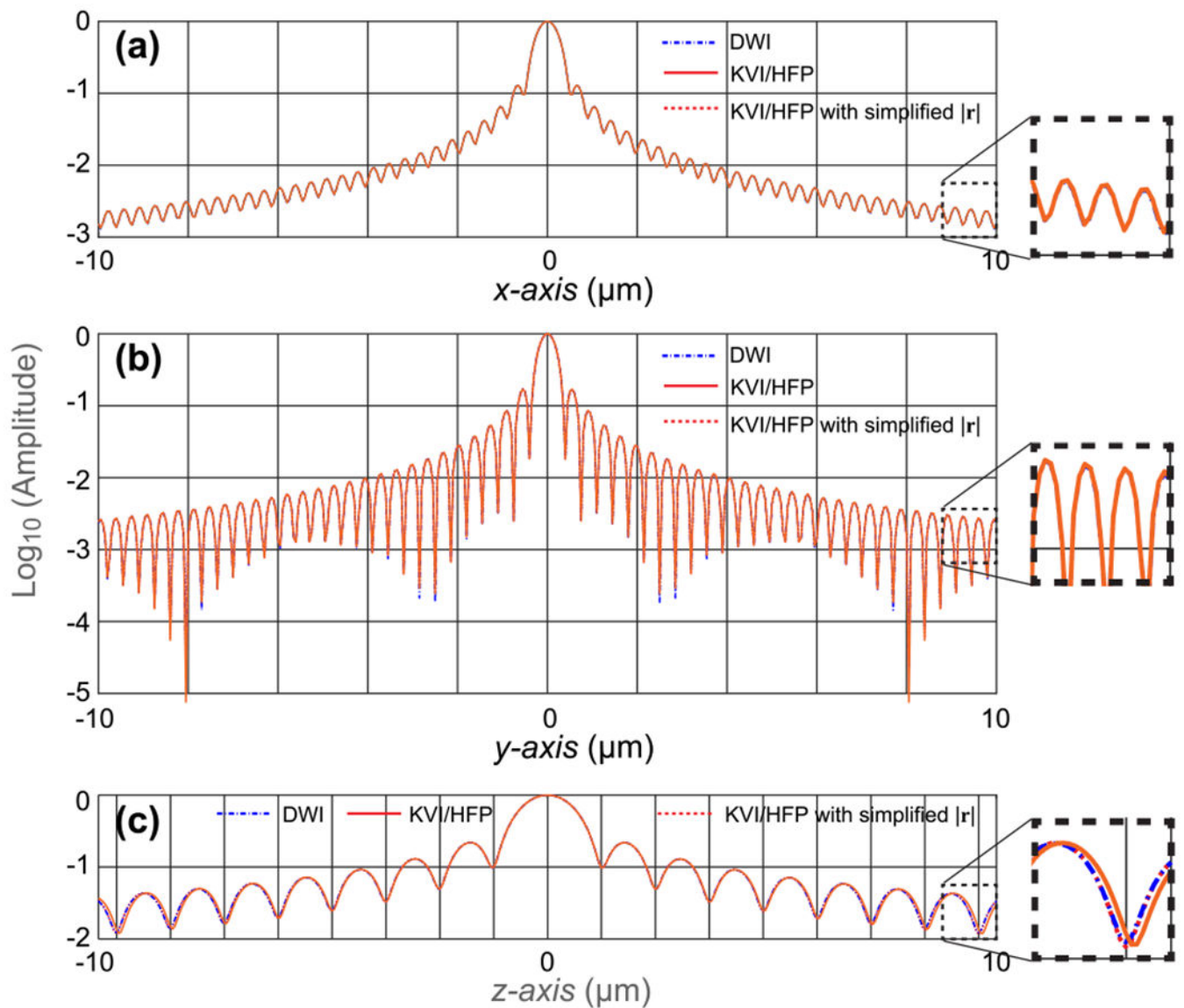
Fig. 6.
Computed focal field amplitudes ($\log_{10}$) along the (a) x axis, (b) y axis, and (c) z axis, using the solution from the DWI (dashed blue), KVI/HFP (solid red), and KVI/HFP with simplified |**r**| in the exponent (dashed red). Since the curves overlap without visible differences, only the KVI/HFP solution is fully visible. Inset on the right magnifies the dashed box located at 10 μm from the focal origin. Incident wavelength is 0.8 μm and NA = 0.866; medium refractive index is 1.333.
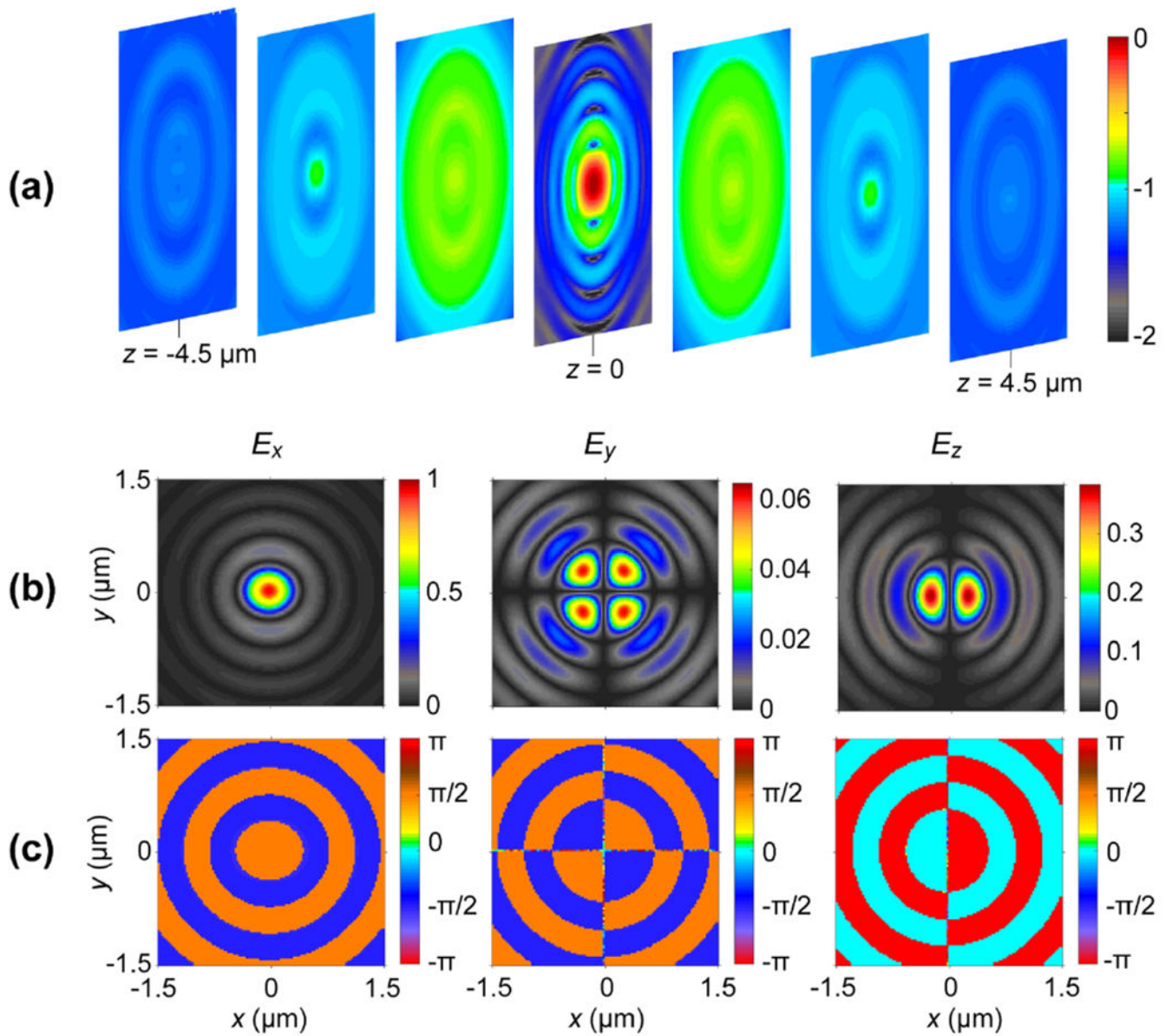
Fig. 7.
Computed electric fields in the focal volume in a non-scattering medium for *x*-polarized incident plane wave. The solution of the HFP is applied to compute (a) amplitude ($\log_{10}$) of selected slices in the focal volume. $x - y$ plane slices are shown at $z = -4.5$ µm, -3 µm, -1.5 µm, $0, 1.5$ µm, 3 µm, and 4.5 µm. (b) Amplitude and (c) phase of electric field components at the focal plane ($z = 0$). Incident wavelength is 0.8 µm and NA = 0.866; medium refractive index is 1.333.
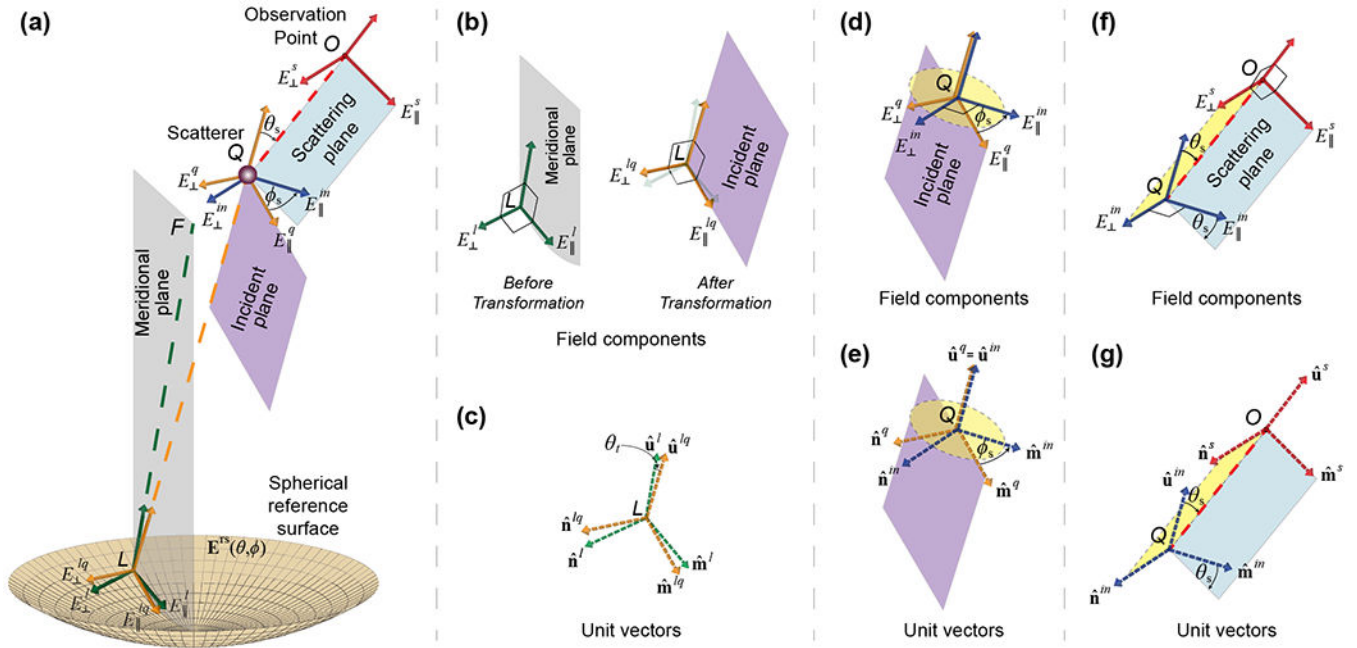
Fig. 8.

Scattering by a single scatterer. (a) Complete process including the electric field at the spherical reference surface (L), incident electric field at the scatterer (Q), and scattered field at the observation point (O). (b) Graphical representation of electric field components $\left(E_\parallel^l, E_\perp^l\right)$ at the spherical reference surface before transformation and $\left(E_\parallel^{lq}, E_\perp^{lq}\right)$ after transformation. $E_\parallel^l$ is parallel to the meridional plane, and $E_\parallel^{lq}$ is parallel to the incident plane. (c) Unit vectors of (b). (d) Graphical representation of incident field at the scatterer relative to the incident plane $\left(E_\parallel^q, E_\perp^q\right)$ and relative to the scattering plane $\left(E_\parallel^{in}, E_\perp^{in}\right)$. (e) Unit vectors of (d). (f) Graphical representation of scattered field at the observation location O. $E_\parallel^{in}$ and $E_\parallel^s$ are parallel, and $E_\perp^{in}$ and $E_\perp^s$ are normal to the scattering plane. (g) Unit vectors of (f). The spherical reference surface is drawn horizontally such that the scattering diagram aligns with the illustrations in other references [15,17,48]. Not to scale.
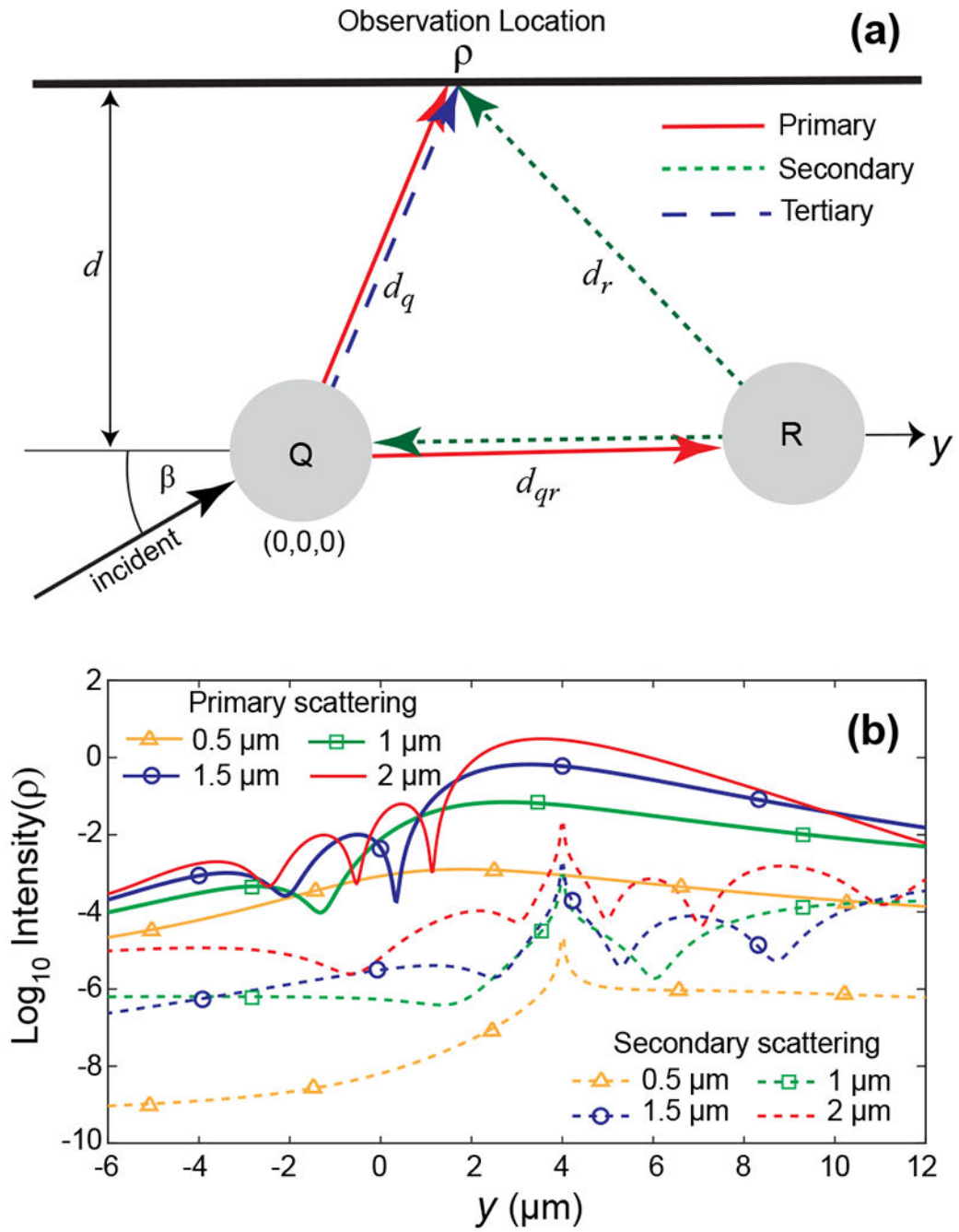
Fig. 9.

(a) Primary, secondary, and tertiary scattering. The scattered field of the Qth scatterer becomes an incident on the Rth scatterer and creates secondary scattering. The secondary scattering reaches the observation location. In addition, it becomes an incident on the Qth scatterer and produces tertiary scattering. d_q is distance from the center of the Qth scatterer to ρ, d_r is distance from the center of the Rth scatterer to ρ, and d_{qr} is distance from the center of the Qth scatterer to the center of the Rth scatterer. (b) $\log_{10}$ intensities of primary (solid) and secondary (dashed) scattering at ρ along the y axis for spherical scatterers of different

sizes. For each simulation, we considered two scatterers of the same size spaced (d_{qr})4 µm apart. $d = 4$ µm and $\beta = 45°$. Four scatterer sizes considered are 0.5 µm, 1 µm, 1.5 µm, and 2 µm.
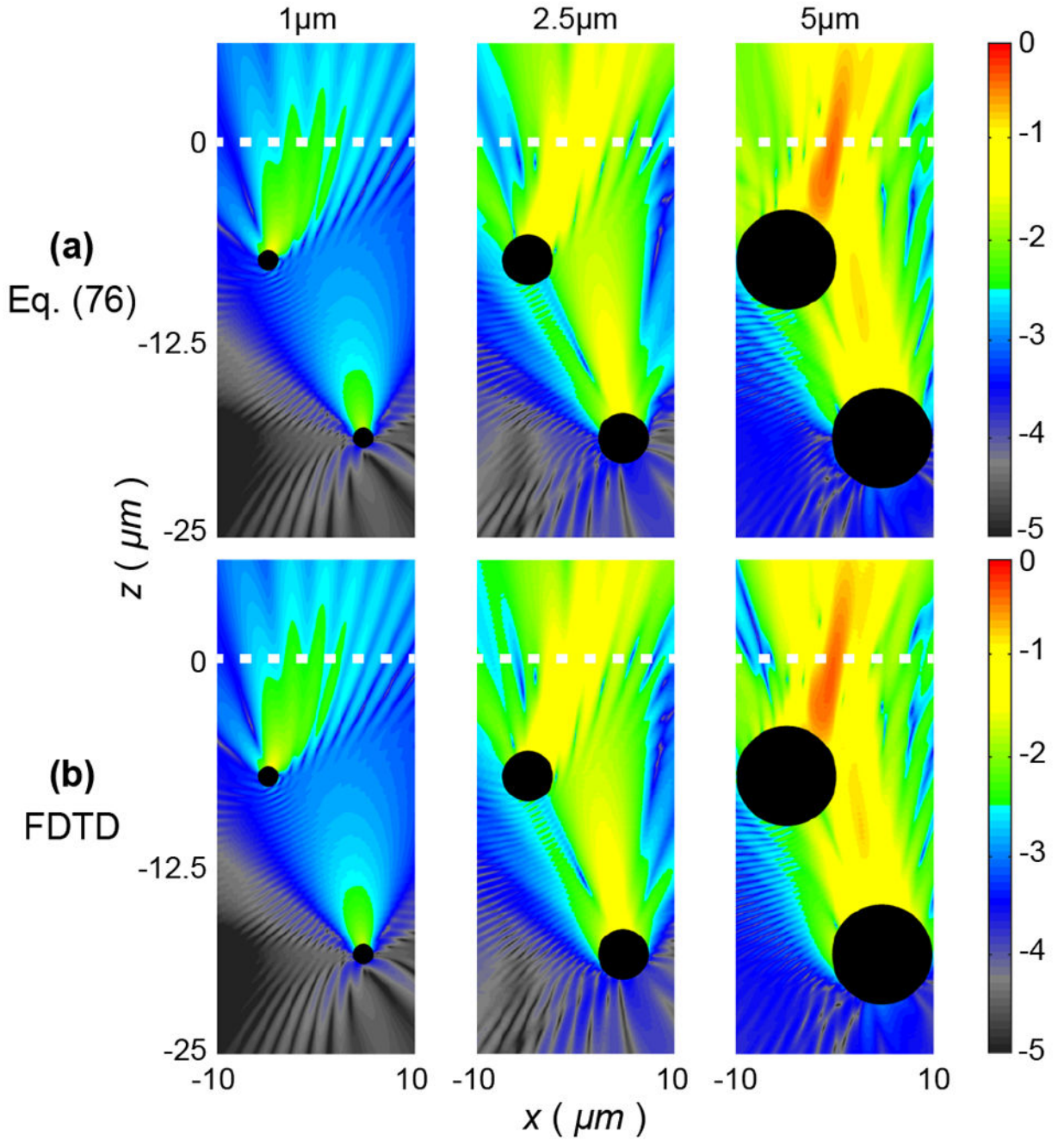
Fig. 10.

x component of the scattered electric field amplitude on the $x - z$ plane ($y = 0$) computed using (a) our method discussed in Section 5 and (b) FDTD for 1.0 µm (left), 2.5 µm (middle), and 5.0 µm (right) spherical scatterers. The scatterers are located at $(-2.4 \ \mu m, 0 \ \mu m, -6 \ \mu m)$ and $(2.4 \ \mu m, 0 \ \mu m, -15 \ \mu m)$. The horizontal dashed line shows the focal plane. Amplitude results are shown in $\log_{10}$ scale. NA of the lens is 0.667.

Table 1.

Comparison of Solution Integrals Provided by DWI, KVI, and HFP[a]

Method	Integral	Eqs.
DWI	$\dfrac{-ik}{2\pi} \int\int_A \dfrac{\exp(i\psi_1)}{f_1} (\mathbf{E}) \, \mathrm{d}A$	(16)
KVI	$\dfrac{-ik}{2\pi} \int\int_A \dfrac{\exp(i\psi_2)}{|\mathbf{r}|} \left(\dfrac{\mathbf{E}\cos\alpha}{2} + \dfrac{\partial \mathbf{E}}{\partial r_0} \dfrac{1}{2ik} \right) \mathrm{d}A$	(25)
HFP	$\dfrac{-ik}{2\pi} \int\int_A \dfrac{\exp(i\psi_2)}{|\mathbf{r}|} \left(\dfrac{\mathbf{E}\cos\alpha}{2} + \dfrac{\mathbf{E}}{2} \right) \mathrm{d}A$	(29)

[a] $\psi_1 = kf_1 + kz\cos\theta - k[\rho\sin\theta\cos(\phi - \varphi)]$, and $\psi_2 = k|\mathbf{r}|$.